Relativistic and nonrelativistic impulse approximation descriptions of 300—1000 MeV proton + nucleus elastic scattering

L. Ray and G. W. Hoffmann
Department of Physics, The University of Texas at Austin, Austin, Texas 78712
(Received 1 October 1984)

Intermediate energy (300—1000 MeV) proton-nucleus elastic observables, obtained using the relativistic and nonrelativistic impulse approximations, are compared to each other and with p+^{40}Ca, ^{48}Ca, and ^{208}Pb data. Systematic, energy dependent differences between the model predictions and the data are observed and discussed. The underlying target densities are then adjusted in each model to obtain best fits to the differential cross section and analyzing power data at each energy. The variations in the resulting effective target density parameters show the deficiencies, with respect to the energy dependence, of the relativistic and nonrelativistic impulse approximations. Improvements which may eliminate some of the energy dependence are discussed.

I. INTRODUCTION

Traditionally, nonrelativistic (NR) microscopic models have been used to describe intermediate energy proton-nucleus (pA) elastic scattering phenomena through use of Schrödinger equation formalisms which include relativistic kinematics. Examples are the multiple scattering series of Watson[1] and Kerman, McManus, and Thaler KMT,[2] the multiple diffraction theory of Glauber,[3] and the Bethe-Goldstone self-energy approach.[4] Such approaches have met with considerable success in reproducing pA data at low and high energies. For instance, NR models with Pauli blocking and binding energy effects included in intermediate projectile—target-nucleon scattering states (i.e., medium effects) lead to good descriptions of pA data at energies less than 300 MeV (Refs. 5 and 6). On the other hand, nonrelativistic impulse approximation (NRIA) models which do not account for nuclear medium effects are reasonably successful at higher energies ($E \geq 800$ MeV) when second-order terms (i.e., those accounting for target nucleon correlations) and electromagnetic spin-orbit corrections are included.[6,7] Thus, until a few years ago, it seemed that accurate, parameter-free descriptions of pA elastic and nonelastic scattering observables would eventually be achieved through use of traditional NR approaches.

This view has now changed owing to the inability of nonrelativistic calculations to account for recent pA elastic scattering data at 500 MeV, particularly the pA spin observables.[6,8,9] Here the general characteristics of the NRIA predictions include differential cross section minima which are too deep relative to the data (see Fig. 1 of Ref. 8), forward angle analyzing power predictions which are much too smooth compared to the rich structure of the data (see Fig. 2 of Ref. 8), and theoretical spin-rotation functions which display too little structure and incorrect magnitudes in comparison with the data (see Fig. 2 of Ref. 10 and Fig. 12 of Ref. 6). Further theoretical improvements in the NR multiple scattering models proved fruitless, however.[8] Alternate density models, different nucleon-nucleon (NN) phase shift solutions, second-order optical potential terms, Fermi motion averaging, Breit frame kinematics and relativistic spin precession in the NN spin dependent effective interactions,[11] electromagnetic spin-orbit corrections,[12] and simple (zero range) Pauli blocking estimates[9] were unable to even qualitatively account for the discrepancies between NR scattering models and the 500 MeV data.

It is perhaps possible that the deficiencies observed at 500 MeV might be overcome by including Pauli blocking and other medium effects which have been shown to be important at lower energies.[4—6] It seems unlikely, however, that such will be the case based on phenomenological investigations of the NR pA effective interaction[13] at 500 MeV and preliminary[14] NR Pauli blocking calculations above pion production threshold which suggest that medium modifications in the NR scattering model are small at 500 MeV.

Motivated by the failure of the NR approaches and the very successful descriptions of intermediate energy pA elastic scattering spin observables obtained by recent Dirac optical model phenomenology,[15] a relativistic impulse approximation (RIA) folding model for the pA Dirac equation optical potential was constructed[16] and subsequently shown to provide a good description of the 500 MeV data.[17,18] Other work demonstrated that the RIA description of pA spin observables is quite successful throughout the intermediate energy range.[19] However, it was also shown that incorrect RIA predictions for the elastic differential cross sections are obtained, particularly for energies less than 400 MeV.[19]

The significant difference between the relativistic and nonrelativistic models originates in the former with the considerable strengths of certain of the components of the NN effective interaction. In Lorentz invariant form these strengths are comparable in magnitude to the nucleon mass,[11] and the strong potentials can permit scattering of the projectile into virtual negative energy states (a characteristic feature of relativistic theories) to make sizable contributions to the elastic scattering process. The strong components of the Lorentz invariant NN effective interaction trace to the importance of scalar and vector

 ©1985 The American Physical Society

meson exchange.[20] The importance of the virtual negative energy states depends on the differences between the vector and scalar potentials which are related, in NR language, to the spin-orbit coupling strength.[16,21] Since the Schrödinger equivalent of the Dirac optical potential[15] contains significant density squared (ρ^2) terms which represent the contributions of intermediate negative energy states of the projectile, the success of the nonrelativistic impulse approximation (NRIA) model at the higher energies is presumably due to the relative weakness of the spin-orbit coupling and to the dominance of the spin-independent absorptive part of the optical potential. The pA distorted wave function is depleted in the high density regions of the nucleus, and the relativistic dynamics (i.e., the ρ^2 terms in the Schrödinger equivalent potential) are suppressed.[16,17] At energies near 500 MeV the spin dependence is greatest relative to the spin independent absorption,[21,22] and the success of relativistic descriptions of the data leaves little doubt as to the need for the inclusion of relativistic dynamics in medium energy pA scattering.

Future theoretical work associated with the relativistic description of pA scattering will most likely focus on meson exchange models for the NN off-shell t matrix and virtual negative energy scattering processes,[23,24] Pauli blocking in intermediate states,[25] and estimates of correlation effects. Field theoretical considerations for pA processes have also begun.[26] Thus it is appropriate at this time to clearly delineate the specific ingredients of the RIA-Dirac equation model and to discuss the successes and failures of the model with respect to the energy dependence of the predicted pA elastic scattering observables.

In Sec. II the details of the RIA optical potential model and Dirac equation approach for pA elastic scattering will be explained. In Sec. III a brief summary of the nonrelativistic impulse approximation optical potential model will be given. The systematics of the energy dependences of the RIA and NRIA models will be presented in two ways in Sec. IV. First, the theoretical p + ^{40}Ca and p + ^{208}Pb elastic observables from 300 to 1000 MeV will be directly compared to available data and to each other. Second, the systematics will be concisely summarized by displaying the energy dependence of the target densities which in the RIA and NRIA models brings about $|\chi|^2$ optimized representations of the data. We also fit 500 and 800 MeV p + ^{48}Ca data and discuss the systematics of the ^{48}Ca−^{40}Ca deduced neutron density differences. Such densities provide a straightforward means of phenomenologically accounting for physical processes not included in the simple RIA and NRIA models. A summary and some conclusions are given in Sec. V.

II. THE RELATIVISTIC IMPULSE-APPROXIMATION–DIRAC-EQUATION MODEL

The relativistic description of the proton-nucleus system should, strictly speaking, be considered within the framework of a relativistic quantum field theory (RQFT) of interacting nucleons and mesons, or perhaps ultimately in terms of quarks and gluons via quantum chromodynamics. Initial development of the former approach is underway,[20,25,26] whereas the latter, more theoretically appealing approach, is computationally intractable at present.

Here we defer consideration of a RQFT approach in favor of a more conventional one which draws upon NR multiple scattering formalisms and heuristic arguments for guidance in forming a relativistic pA optical potential in terms of NN scattering phenomenology and ground state nuclear structure properties. The development of the general form of the relativistic optical potential will be presented first, followed by a discussion of kinematics, the relativistic invariant NN effective interactions, target densities, the explicit evaluation of the optical potential, and the Dirac equation as applied to pA elastic scattering.

A. Theoretical basis and model prescriptions

In order to maintain contact with previous nonrelativistic scattering theories,[1,2] while at the same time incorporating some degree of Lorentz invariance, we initially follow an approach analogous to that in Ref. 27. The target is treated nonrelativistically, and the projectile proton is described via the one-body, Dirac Hamiltonian; thus we have the following semirelativistic equation of motion for the pA system:

$$\left[\boldsymbol{\alpha}\cdot\mathbf{p}+\beta\left[m+\sum_{i=1}^{A}v_{pi}\right]+H_A\right]\Psi=E\Psi\ . \tag{1}$$

In this equation $\boldsymbol{\alpha}$, β are the usual Dirac matrices,[28] m is the proton mass, v_{pi} denote the projectile-target nucleon interactions, H_A is the nonrelativistic, many-body target nucleus Hamiltonian, and we assume that the projectile and target nucleons are distinct so that Ψ may be factored into a product of a four-component wave function for the projectile times a nonrelativistic many-body Schrödinger wave function for the target nucleus. The target kinetic energy operator is neglected, thus deferring recoil and target current corrections for later work. Defining the pA propagator as

$$G=(\not{p}-m-\gamma^0 H_A+i\epsilon)^{-1}\ , \tag{2}$$

where $\not{p}\equiv\gamma_\mu p^\mu$ and γ_μ are the usual Dirac γ matrices,[28] leads to a many-body Lippmann-Schwinger version of Eq. (1) given by

$$T=\sum_{i=1}^{A}v_{pi}+\sum_{i=1}^{A}v_{pi}GT\ . \tag{3}$$

Equation (3) has the same schematic form as does the standard nonrelativistic many-body Lippmann-Schwinger equation. However, the new definitions of v_{pi}, G, and T introduced here are to be noted. Selecting antisymmetric (physical) intermediate target states in Eq. (3) results in

$$T=Av+AvG\mathring{A}T\ , \tag{4}$$

where $\mathring{A}$ projects antisymmetric target nucleus states and v represents an averaged projectile-target nucleon interaction. This is analogous to the Kerman, McManus, and Thaler (KMT) (Ref. 2) and Watson[1] nonrelativistic multiple scattering theories. Clearly, a one-body relativistic

(for the projectile), many-body nonrelativistic (for the target) effective operator τ can be introduced where

$$\tau = v + vGQ\tau \ . \tag{5}$$

Here $\mathring{A} = P + Q$, and $P = |\Phi_{\text{g.s.}}\rangle\langle\Phi_{\text{g.s.}}|$ projects the nuclear ground state channel; $|\Phi_{\text{g.s.}}\rangle$ is the antisymmetric target nucleus ground state wave function. Introducing the pA optical potential for elastic scattering through the definition,

$$PTP = U_{\text{opt}} + U_{\text{opt}} G\, PTP \ , \tag{6}$$

allows U_{opt} to be related to τ according to the usual form:

$$U_{\text{opt}} = AP\tau P + A(A-1)P\tau QGQ\tau P + \cdots \ , \tag{7}$$

in analogy with NR multiple scattering theory. To obtain pA observables we therefore solve the one-body Dirac equation,

$$(\not{p} - m - \gamma^0\epsilon_0 - U_{\text{opt}})\phi_{\text{p}}(\mathbf{r}) = 0 \ , \tag{8}$$

where $P\Psi = \Psi_{\text{g.s.}} = \phi_{\text{p}}(\mathbf{r})\Phi_{\text{g.s.}}$ and $H_A\Phi_{\text{g.s.}} = \epsilon_0\Phi_{\text{g.s.}}$. Suitable approximations for U_{opt} must be provided to proceed further. The preceding discussion mainly serves to emphasize the close similarity between the NR multiple scattering formalism of Watson[1] and one which accounts for relativity of the projectile. Equations (7) and (8) are equivalent to Eq. (1).

The principal limitation in the preceding formalism is the NR treatment of the target nucleus. The utility of such an approach becomes particularly questionable in the evaluation of τ which in the NN center-of-momentum system (c.m.) requires that one of the nucleons be described with a Dirac Hamiltonian, while the other is treated nonrelativistically. To circumvent this discriminative treatment of the two-body subsystem in the pA scattering process and to permit a numerical study of the sensitivity of pA scattering observables to relativistic aspects of the target nucleus, we have arbitrarily replaced the nonrelativistic target wave function, $|\Phi_{\text{g.s.}}\rangle$, with a relativistic wave function $|\tilde{\Phi}_{\text{g.s.}}\rangle$ which is discussed in the following.[29] In addition, the complicated, semirelativistic, effective operator τ is replaced by the free NN scattering t matrix Υ_i (in the appropriate Dirac representation), and the second- and higher-order correlation terms in U_{opt} in Eq. (7) are dropped. Thus the optical potential used in Eq. (8) is of the form

$$U^{(1)}_{\text{opt}} = \sum_{i=1}^{A} \langle \tilde{\Phi}_{\text{g.s.}} | \Upsilon_i | \tilde{\Phi}_{\text{g.s.}} \rangle \ . \tag{9}$$

B. Kinematics

In momentum space the optical potential of Eq. (9) involves a convolution of off-shell matrix elements of the two-body t matrix with the one-body target density matrix,

$$U^{(1)}_{\text{opt}}(\mathbf{k}'_0,\mathbf{k}_0) = (2\pi)^{-3} \int\int\int d^3r'_1 d^3r_1 d^3k_1 e^{i\mathbf{q}\cdot\mathbf{r}'_1} e^{i\mathbf{k}_1\cdot(\mathbf{r}'_1-\mathbf{r}_1)} \sum_\beta \langle \mathbf{k}'_0,\mathbf{k}_1+\mathbf{q} | \Upsilon_\beta | \mathbf{k}_1,\mathbf{k}_0\rangle \rho_\beta(\mathbf{r}'_1,\mathbf{r}_1) \ , \tag{10}$$

where $\mathbf{k}_0$ and $\mathbf{k}'_0$ represent the initial and final projectile momentum space coordinates, $\langle\Upsilon_\beta\rangle$ represent fully off-shell t-matrix elements, $\rho_\beta(\mathbf{r},\mathbf{r}')$ are one-body target density matrices, $\mathbf{q} = \mathbf{k}_0 - \mathbf{k}'_0$ and the sum over the subscript (β) recognizes the differing Lorentz character and isospin dependence of the two-body interaction.[11,21] For application in proton-nucleus scattering it is reasonable to simplify Eq. (10) by neglecting the dependence of $\langle\Upsilon_\beta\rangle$ on the incident target nucleon momentum $\mathbf{k}_1$; we therefore use the so-called "factorized" optical potential form,

$$U^{(1)}_{\text{opt}}(\mathbf{k}'_0,\mathbf{k}_0) = \sum_\beta \langle \mathbf{k}'_0,\boldsymbol{\kappa}+\mathbf{q} | \Upsilon_\beta | \boldsymbol{\kappa},\mathbf{k}_0\rangle \tilde{\rho}_\beta(\mathbf{q}) \ , \tag{11}$$

where $\boldsymbol{\kappa}$ is a momentum parameter for the struck target nucleon, chosen so as to best approximate the original integral in Eq. (10).

In Ref. 11 it is pointed out that for the case of on-shell matrix elements of $U^{(1)}_{\text{opt}}$, $\boldsymbol{\kappa}$ should be chosen such that the elementary two-body scattering operator is also evaluated on shell. The value of $\boldsymbol{\kappa}$ can be obtained by requiring (refer to Fig. 1)

$$|\bar{\mathbf{k}}_0| = |\bar{\mathbf{k}}'_0| \ ,$$
$$|-\bar{\mathbf{k}}_0/A + \mathbf{x}| = |-\bar{\mathbf{k}}_0/A + \mathbf{x} + \mathbf{q}| \ . \tag{12}$$

Thus $\mathbf{x} = (\mathbf{q}/2)(1/A - 1)$ and

$$\boldsymbol{\kappa} = -\bar{\mathbf{k}}_0/A + (\mathbf{q}/2)(1/A - 1) \ ,$$

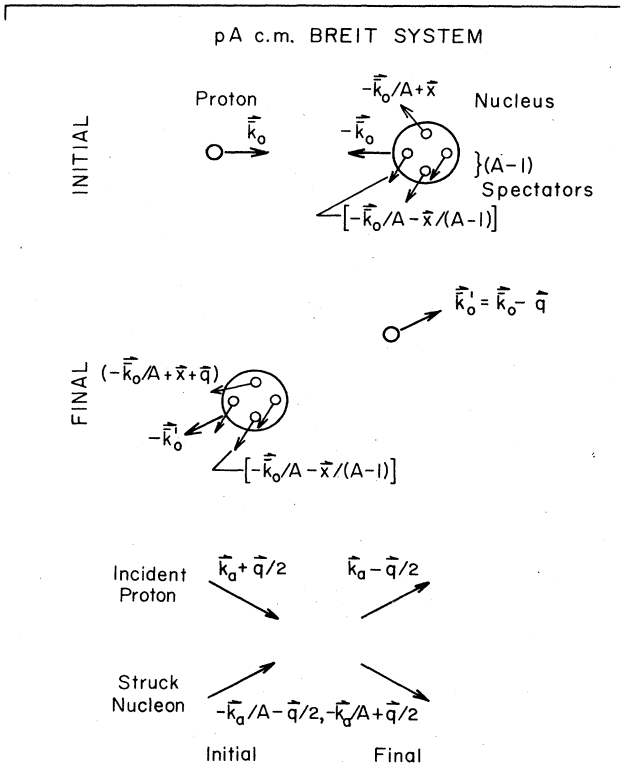

FIG. 1. Breit frame kinematics.

where $\bar{\mathbf{k}}_0$ is the pA c.m. momentum corresponding to an incident laboratory energy $T_{\rm lab}$. Introducing the average momentum $\mathbf{k}_a \equiv (\bar{\mathbf{k}}_0 + \bar{\mathbf{k}}'_0)/2$ and momentum transfer $\mathbf{q} = \bar{\mathbf{k}}_0 - \bar{\mathbf{k}}'_0$, we obtain the convenient kinematic values for the projectile proton and struck nucleon in the pA center-of-momentum reference frame given in the lower portion of Fig. 1. A significant result of this choice of kinematics is that the two-body c.m. energy depends on the selected momentum transfer; hence two-body on-shell scattering information covering a broad energy range above the value of $T_{\rm lab}$ is required. Furthermore, on-shell matrix elements of Υ_β are defined for all on-shell pA kinematic values. The following equations include the relevant kinematic quantities for elastic scattering in this so-called Breit kinematic frame:[11]

$$s_{\rm Breit} = (E_{\rm p} + E_{\rm SN})^2 - k_a^2 (1 - 1/A)^2 , \tag{13a}$$

$$E_{\rm p} = (k_a^2 + q^2/4 + m^2)^{1/2} , \tag{13b}$$

$$E_{\rm SN} = [(k_a/A)^2 + q^2/4 + m^2]^{1/2} , \tag{13c}$$

$$k_a = (\bar{k}_0^{\,2} - q^2/4)^{1/2} , \tag{13d}$$

$$t = -q^2 , \tag{13e}$$

and

$$T_{\rm lab,eff}(NN) = \frac{s_{\rm Breit}}{2m} - 2m . \tag{13f}$$

In Eqs. (13) $s_{\rm Breit}$ is the invariant two-body total energy squared, $E_{\rm p}$ and $E_{\rm SN}$ are the projectile proton and struck nucleon total energies, m is the nucleon mass, and $T_{\rm lab,eff}$(NN) denotes the equivalent laboratory kinetic energy for NN elastic scattering corresponding to the total energy squared, $s_{\rm Breit}$. We note that $T_{\rm lab,eff}(\mathrm{NN}) \geq T_{\rm lab}$ and that its value monotonically increases with q. For example, for 800 MeV proton scattering from ^{208}Pb, calculation of the on-shell portion of the optical potential from 0 to 3 fm^{-1} requires NN phase shifts ranging from 800 to 977 MeV.

C. Projectile-target nucleon, relativistic effective interaction

The basic premise of the impulse approximation is that the free scattering NN t matrix provides a reasonable estimate of the two-body effective interaction needed to generate the optical potential. It is customary in nuclear physics to express the NN scattering amplitudes in the Pauli spin matrix representation involving five independent terms given by[30]

$$f(q) = A(q) + B(q)\sigma_{1n}\sigma_{2n} + C(q)(\sigma_{1n} + \sigma_{2n}) + D(q)\sigma_{1q}\sigma_{2q} + E(q)\sigma_{1p}\sigma_{2p} , \tag{14}$$

where $\sigma_{ix} \equiv \boldsymbol{\sigma}_i \cdot \hat{x}$, $\hat{n} = (\mathbf{k}\times\mathbf{k}')/|\mathbf{k}\times\mathbf{k}'|$, $\hat{q} = (\mathbf{k}-\mathbf{k}')/|\mathbf{k}-\mathbf{k}'|$, $\hat{p} = (\mathbf{k}+\mathbf{k}')/|\mathbf{k}+\mathbf{k}'|$, $\mathbf{k}$ and $\mathbf{k}'$ are the initial and final NN c.m. momenta, $\mathbf{q} = \mathbf{k} - \mathbf{k}'$, and the subscripts 1 and 2 refer to the incident and target nucleon, respectively.

In order to reexpress the preceding NN phenomenology in a form which displays the proper Lorentz transformation character, the following Lorentz invariant form has been proposed for NN scattering:[11]

$$\hat{F}(s,t) = F_S(s,t) I_1 I_2 + F_P(s,t)\gamma_1^5\gamma_2^5 + F_V(s,t)\gamma_1^\mu\gamma_{2\mu} + F_A(s,t)\gamma_1^5\gamma_1^\mu\gamma_{2\mu}^5 + F_T(s,t)\sigma_1^{\mu\nu}\sigma_{2\mu\nu} \equiv \sum_\beta \hat{F}_\beta(s,t) 0_{1\beta} 0_{2\beta} . \tag{15}$$

This form is analogous to that used in β decay studies.[31] The conventional Mandelstam kinematic quantities are denoted by (s,t), while I (unit), γ^5, γ_μ, $\gamma^5\gamma_\mu$, and $\sigma_{\mu\nu}$ are the usual 16 linearly independent 4×4 matrices.[28] The $\hat{F}_\beta$ represent F_S, F_P, etc., while $0_{i\beta}$ represent I_i, γ_i^5, etc., for $i = 1,2$. Within the positive energy NN sector we may relate the two representations for NN elastic scattering by requiring

$$\bar{u}_{s_1'}(\mathbf{k}')\bar{u}_{s_2'}(-\mathbf{k}')\hat{F}(s,t)u_{s_1}(\mathbf{k})u_{s_2}(-\mathbf{k}) = \chi_{s_1'}^\dagger \chi_{s_2'}^\dagger f(s,t)/P_{\rm NN,\,c.m.}(s_{\rm Breit})\chi_{s_1}\chi_{s_2} , \tag{16}$$

where $P_{\rm NN,\,c.m.}(s_{\rm Breit})$ is the NN c.m. momentum corresponding to $s_{\rm Breit}$ of Eq. (13a) and $u_s(\mathbf{k})$, given by

$$u_s(\mathbf{k}) = [(E+m)/(2m)]^{1/2} \begin{bmatrix} 1 \\ \dfrac{\boldsymbol{\sigma}\cdot\mathbf{k}}{E+m} \end{bmatrix} \chi_s , \tag{17}$$

denotes the positive energy Dirac spinor with $E = (k^2 + m^2)^{1/2}$. In Eq. (17) χ_s represents a two-component Pauli spinor. Simply stated, Eq. (16) requires that equivalent scattering probability amplitudes be maintained in the two representations for the initial and final spin configurations of the NN system. This relation permits the assignment of values for each component of $\hat{F}$ in terms of the Pauli representation of the NN scattering amplitude. Specifically, a 5×5 matrix equation can be obtained which relates the Pauli amplitudes $\{A,B,C,D,E\}$ to the invariant amplitudes $\{F_S,F_P,F_V,F_A,F_T\}$ for given on-shell kinematic values s and t. This matrix equation is given by[11]

$$\begin{bmatrix} A \\ B \\ C \\ D \\ E \end{bmatrix}_{s,t} = B_1 \begin{bmatrix} F_S \\ F_P \\ F_V \\ F_A \\ F_T \end{bmatrix}_{s,t} , \tag{18}$$

where explicit values for the B_1 matrix are provided in Tables I and II of Ref. 11.

It should be emphasized that the form of the invariant NN amplitude of Eq. (15) is not complete. Other momentum dependent terms[32] can be introduced which affect the off-shell dependence of $\hat{F}$ in the positive energy NN sub-

space. More importantly, other classes of invariant terms can be added to the expression for $\hat{F}$ which do not contribute to the positive energy matrix elements in Eq. (16), but which would contribute to matrix elements of $\hat{F}$ involving negative energy states of either particles 1, 2 or both.[24] These additional components of $\hat{F}$ will contribute to the proton-nucleus scattering through their effects on the optical potential. Intermediate scattering of the projectile through virtual negative energy states, an important process for medium energy pA scattering, would be directly affected by additional terms in $\hat{F}$ of this latter type.[33] These considerations are expanded in Appendix A.

Since the NN data constrain only the on-shell, positive energy portion of $\langle \hat{F} \rangle$, theoretical models of the NN interaction are needed to provide off-shell and negative energy matrix elements of $\hat{F}$. Until reliable model calculations of $\hat{F}$ are available, Eq. (15) must suffice as a reasonable starting point for the first generation of relativistic microscopic optical model calculations.

The points mentioned previously and in Appendix A are fairly obvious, but are belabored here in order to properly qualify the model under consideration and to provide a connection with previous nonrelativistic models which, roughly speaking, correspond to retention of only the first term in Eq. (A3) in Appendix A.

Finally, the usual local prescription for the pA optical potential is used. We set

$$U_{\rm opt}^{(1)}(\mathbf{k}'_0,\mathbf{k}_0) \cong \sum_\beta \Upsilon_\beta(q)\tilde{\rho}_\beta(q) , \tag{19}$$

with $\mathbf{q}=\mathbf{k}_0-\mathbf{k}'_0$ and $\Upsilon_\beta(q)$ is evaluated on shell. Such localization prescriptions for pA elastic scattering at intermediate energies were investigated by Picklesimer *et al.*[34] and found to be inadequate only for large momentum transfers well beyond the region considered here.

The localized NN scattering operator Υ_β in the pA Breit kinematic frame is obtained from the invariant amplitude $\hat{F}$ by considering the general expression for an arbitrary two-fermion scattering cross section. The result obtained in Eq. (B5) in Appendix B is

$$\Upsilon_\beta(q) = -2\pi \frac{(\hbar c)^2}{m} \frac{R(q)}{R(0)} P_{\rm lab} \hat{F}_\beta(q) , \tag{20}$$

where $R(q)$, involving various kinematic quantities, is given in Appendix B, $P_{\rm lab}$ is the laboratory momentum for the incident proton, and the invariant amplitudes introduced in Eq. (15) have been inserted. The subscripts β account for the Lorentz structure and isospin dependence of the scattering amplitudes.

D. The RIA optical potential and the Dirac equation for pA scattering

The RIA optical potential model is evaluated starting with [see Eq. (9)]

$$U_{\rm opt}^{(1)}(q) = \sum_\beta \sum_{i=1}^{A} \langle \tilde{\Phi}_{\rm g.s.} \mid \Upsilon_{\beta i}(q) \mid \tilde{\Phi}_{\rm g.s.} \rangle , \tag{21}$$

where (i) denotes the target nucleon label. The antisymmetrized, relativistic nuclear wave function is expanded as

$$\tilde{\Phi}_{\rm g.s.}(\mathbf{r}_1 \cdots \mathbf{r}_A) = \frac{1}{\sqrt{A!}} \det \prod_{i=1}^{A} \zeta_{\{\alpha\}}(\mathbf{r}_i) , \tag{22}$$

where

$$\zeta_{\{\alpha\}}(\mathbf{r}_i) = \begin{bmatrix} \phi_{nlj}(r) \\ -i\boldsymbol{\sigma}\cdot\hat{r}\lambda_{nlj}(r) \end{bmatrix} \mathscr{Y}_{lj}^{\mu}(\hat{r}) \tag{23}$$

represents the four-component Dirac single particle wave function for the $\{\alpha\}=(n,l,j)$ orbital. The set of $\{\alpha\}$ includes all occupied single particle subshells. The spin-angle function $\mathscr{Y}_{lj}^{\mu}(\hat{r})$ is given as usual by

$$\mathscr{Y}_{lj}^{\mu}(\hat{r}) = \sum_{m_s} (l,\mu+m_s,\tfrac{1}{2},-m_s \mid j\mu) Y_l^{\mu+m_s}(\hat{r}) \chi_{1/2,-m_s} . \tag{24}$$

Inserting Eqs. (15), (20), and (22) into Eq. (21) yields, for spin zero nuclei with filled (l,j) subshells (such as ^{40}Ca, ^{48}Ca, and ^{208}Pb),

$$U_{\rm opt}^{(1)}(r) = -\frac{2\pi(\hbar c)^2}{m} \frac{R(q)}{R(0)} P_{\rm lab} \times [U_S(r) + \gamma_1^0 U_V(r) - 2i\boldsymbol{\alpha}_1\cdot\hat{r} U_T(r)] , \tag{25a}$$

where subscript 1 refers to the projectile proton. The individual potentials are given by

$$U_S(r) = (2\pi)^{-3} \sum_{i={\rm p,n}} \int d^3q\, e^{-i\mathbf{q}\cdot\mathbf{r}} F_S^{(i)}(q) \tilde{\rho}_S^{(i)}(q) , \tag{25b}$$

$$U_V(r) = (2\pi)^{-3} \sum_{i={\rm p,n}} \int d^3q\, e^{-i\mathbf{q}\cdot\mathbf{r}} F_V^{(i)}(q) \tilde{\rho}_V^{(i)}(q) , \tag{25c}$$

and

$$U_T(r) = (2\pi)^{-3} \sum_{i={\rm p,n}} r \int d^3q\, e^{-i\mathbf{q}\cdot\mathbf{r}} F_T^{(i)}(q) \tilde{\rho}_T^{(i)}(q) . \tag{25d}$$

In Eq. (25a) the three terms on the right-hand side correspond to scalar, vector, and tensor contributions, while $\tilde{\rho}_S^{(i)}$, $\tilde{\rho}_V^{(i)}$, and $\tilde{\rho}_T^{(i)}$ represent the scalar, vector, and tensor density form factors, respectively. These are given by

$$\tilde{\rho}_S^{(i)}(q) = \int d^3r\, e^{i\mathbf{q}\cdot\mathbf{r}} \rho_S^{(i)}(r) , \tag{26a}$$

$$\tilde{\rho}_V^{(i)}(q) = \int d^3r\, e^{i\mathbf{q}\cdot\mathbf{r}} \rho_V^{(i)}(r) , \tag{26b}$$

and

$$\tilde{\rho}_T^{(i)}(q) = \int d^3r\, e^{i\mathbf{q}\cdot\mathbf{r}} \frac{1}{r} \rho_T^{(i)}(r) . \tag{26c}$$

The superscript i denotes target protons or neutrons. In terms of the upper and lower components of the nuclear wave function these densities are given by

$$\rho_S^{(i)}(r) = \sum_{nlj} \frac{2j+1}{4\pi} (\mid \phi_{nlj} \mid^2 - \mid \lambda_{nlj} \mid^2) , \tag{27a}$$

$$\rho_V^{(i)}(r) = \sum_{nlj} \frac{2j+1}{4\pi} (\mid \phi_{nlj} \mid^2 + \mid \lambda_{nlj} \mid^2) , \tag{27b}$$

and

$$\rho_T^{(i)}(r)=2\sum_{nlj}\frac{2j+1}{4\pi}\phi_{nlj}\lambda_{nlj}\ , \tag{27c}$$

where the sums include occupied proton or neutron orbitals. For the numerical calculations discussed later, the amplitudes and the density form factors were computed to 4 fm^{-1}, and the optical potential [Eqs. (25)] was inserted into the Dirac equation for protons,

$$\left\{\boldsymbol{\alpha}_1\cdot\mathbf{p}+\beta_1[m+U_S(r)]+[U_V(r)+U_{\rm Coul}(r)]-i\beta\boldsymbol{\alpha}_1\cdot\hat{r}\left[2U_T(r)+\frac{\kappa_{\rm p}}{2m}\frac{\partial}{\partial r}U_{\rm Coul}(r)\right]\right\}\phi_{\rm p}(\mathbf{r})=E\phi_{\rm p}(\mathbf{r})\ . \tag{28}$$

In Eq. (28) $U_{\rm Coul}(r)$ represents the spin independent pA Coulomb interaction, $\kappa_{\rm p}$ is the proton anomalous magnetic moment, $\phi_{\rm p}(\mathbf{r})$ is the four-component projectile proton wave function, and E is the total relativistic energy of the incident proton in the pA c.m. frame. The solution of Eq. (28) together with the asymptotic boundary conditions for $\phi_{\rm p}(\mathbf{r})$ gave the pA scattering amplitude from which elastic scattering observables were constructed.[35]

E. NN phase shifts and target densities

For the calculations discussed here, the SP82 phase shift solution of Arndt[21] provided the NN amplitudes needed in Eqs. (14) and (18). The Breit frame NN invariant amplitudes were computed at each laboratory energy using Eqs. (13) and (18). The variation in NN c.m. energy with pA momentum transfer was included in the calculations by inputting NN c.m. amplitudes at five energies ranging from $T_{\rm lab}$ to ($T_{\rm lab}+200$ MeV) and numerically interpolating for specific $T_{\rm lab,eff}$(NN).

The RIA optical potential model specified in Eqs. (25)—(27) requires six separate target densities corresponding to scalar, vector, and tensor distributions for both protons and neutrons. With the exception of the proton-vector density all of these were obtained from theoretical models. The dependence of the RIA predictions on these theoretical nuclear structure models was minimized, however, by the method discussed in the following.

For the calculations discussed here the proton-vector densities for ^{40}Ca, ^{48}Ca, and ^{208}Pb were obtained by unfolding the single proton (free space) electric form factor from the nuclear charge density.[36,37] Corrections for the neutron electric form factor and the nucleon magnetic form factor contributions (in the ^{48}Ca and ^{208}Pb cases) to the apparent total nuclear charge density were also made.[7,38] The theoretical neutron vector density used in the absolute RIA predictions was taken as

$$\rho_V^{\rm n}(r)\,|_{\rm theory}=\rho_V^{\rm p}(r)+[\rho_{\rm n}(r)-\rho_{\rm p}(r)]_{\rm HFB}\ , \tag{29}$$

where the neutron and proton densities in the square brackets are the mean field, Hartree-Fock-Bogoliubov (HFB) distributions of Dechargé and Gogny.[39] This prescription therefore relied on theoretical models for the neutron-proton density difference only; the actual neutron-vector density was "scaled" to experiment [i.e., to the $\rho_V^{\rm p}(r)$ from electromagnetic studies] via Eq. (29). The nonrelativistic HFB neutron-proton density differences are preferred over the Dirac-Hartree neutron-proton vector density differences of Horowitz and Serot since the former account for exchange, pairing effects, and long range correlations via the random-phase approximation (RPA) method, whereas the latter do not.

In order to fit the *differential cross section* data, the form of $\rho_V^{\rm n}(r)$ was taken as

$$\rho_V^{\rm n}(r)=\rho_V^{\rm n}(r)\,|_{\rm theory}+\left\{\frac{\rho_0'}{1+\exp[(r-c)/z]}-\frac{\rho_0}{1+\exp[(r-c_{\rm STD})/z_{\rm STD}]}\right\}, \tag{30}$$

where ρ_0 and ρ_0' are constants that normalize each Woods-Saxon term, $c_{\rm STD}$ and $z_{\rm STD}$ were fixed to reproduce the surface region of $\rho_V^{\rm n}(r)\,|_{\rm theory}$, and (c, z) were adjusted to minimize the $|\chi|^2$ of the fit to the data at each available energy. The values ($c_{\rm STD}$, $z_{\rm STD}$) are (3.451, 0.534) fm, (3.853, 0.500) fm, and (6.631, 0.658) fm for ^{40}Ca, ^{48}Ca, and ^{208}Pb, respectively.

The scalar densities for the parameter free RIA predictions or for the fits to the cross section data were obtained from

$$\rho_S^{(i)}(r)=\rho_V^{(i)}(r)+[\rho_S^{(i)}(r)-\rho_V^{(i)}(r)]_{\rm Serot}\ , \tag{31}$$

where (i) represents protons or neutrons, and the densities in the square brackets were provided by the Dirac-Hartree mean field model of Horowitz and Serot.[29] Whenever $\rho_V^{\rm n}(r)$ was varied according to Eq. (30) in the fitting procedure, $\rho_S^{\rm n}(r)$ was recomputed according to Eq. (31) at each step.

It is also of interest to study the sensitivity and energy dependent systematics of the scalar-vector density difference. In order to explore this feature of the RIA model, the form of $\rho_S^{(i)}(r)$ in Eq. (31) was generalized to

$$\rho_S^{(i)}(r)=\rho_V^{(i)}(r)+\xi\left[[\rho_S^{(i)}(r)-\rho_V^{(i)}(r)]_{\rm Serot}+\frac{[\rho_S^{(i)}(0)-\rho_V^{(i)}(0)]_{\rm Serot}}{1+\exp[(r-c_{\rm STD})/z_{\rm STD}]}\times\left\{\frac{1}{1+\exp[(r-\bar{R})/z_{\rm STD}]}-\frac{1}{1+\exp[(r-c_{\rm STD})/z_{\rm STD}]}\right\}\right]. \tag{32}$$

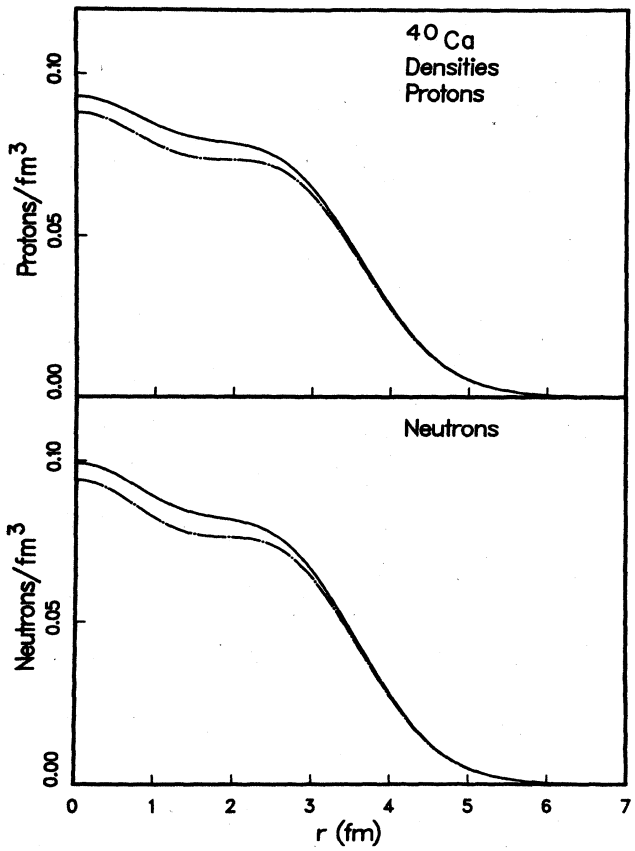

FIG. 2. Point densities for ^{40}Ca used in the parameter-free calculations. Protons and neutrons are in the upper and lower portions, respectively. The baryon (vector) densities are indicated by solid curves; the scalar by dash-dot lines.

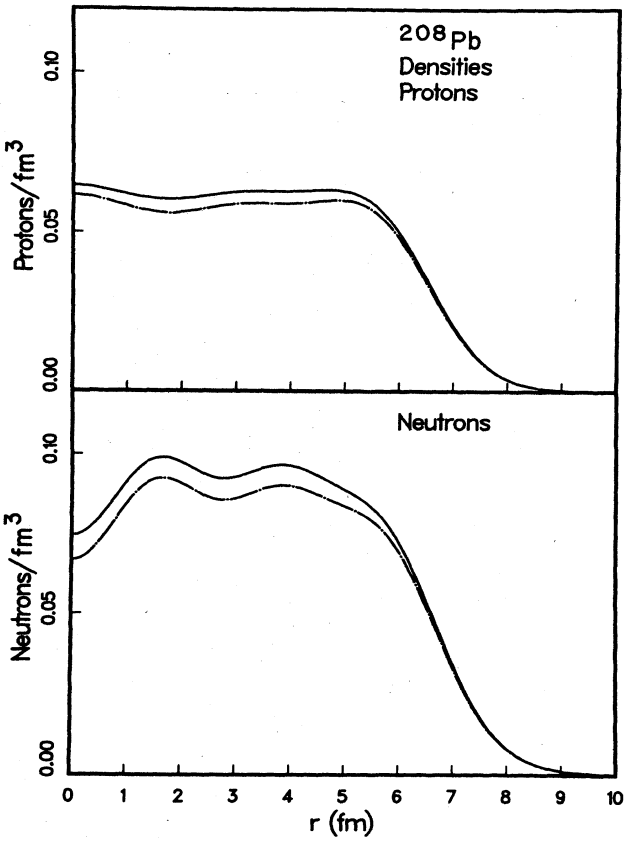

FIG. 3. Same as Fig. 2, except for ^{208}Pb.

In Eq. (32) $c_{\rm STD}$ and $z_{\rm STD}$ were fixed to the same values as in Eq. (30), while $(\xi,\bar{R})$ were adjusted to optimize the fit to the *analyzing power* (A_y) data. Variation of ξ allows one to study the effects of the overall strength of the lower components of the target wave function [see Eq. (27)], while deviation of $\bar{R}$ from $c_{\rm STD}$ examines the sensitivity to the radial variation of the scalar-vector density difference. The parametrization of $\rho_S^{(i)}(r)$ in Eq. (32) ensured that $\rho_S^{(i)}(r)<\rho_V^{(i)}(r)$ for all values of $\bar{R}$ (with $\xi>0$). The same values of ξ and $\bar{R}$ were assumed for proton and neutron scalar densities.

Previous work[40] investigated the contribution of the nuclear tensor potential to pA scattering using the tensor densities of Horowitz and Serot[29] for several nuclei and proton laboratory energies. The effects on the observables were found to very slight; hence $U_T(r)$ was omitted in all the calculations discussed here.

The following summarizes the densities used in the various calculations discussed in Sec. IV. The proton-vector densities were always fixed via electromagnetic measurements. The absolute RIA predictions used the $\rho_V^{\rm n}$ in Eq. (29) and $\rho_S^{(i)}$ from Eq. (31). In obtaining fits to the differential cross sections, Eq. (30) for $\rho_V^{\rm n}$ and Eq. (31) for $\rho_S^{(i)}$ were employed. The analyzing power fits utilized Eq. (29) for $\rho_V^{\rm n}$ together with Eq. (32) for $\rho_S^{(i)}$. The radial distributions of the proton and neutron, vector and scalar point densities used in the absolute RIA predictions are displayed in Figs. 2 and 3 for ^{40}Ca and ^{208}Pb, respectively.

III. THE NONRELATIVISTIC IMPULSE APPROXIMATION OPTICAL POTENTIAL

The nonrelativistic impulse approximation (NRIA) optical potential, based on the Kerman, McManus, and Thaler (KMT) (Ref. 2) formalism, was computed according to the methods discussed in Ref. 7. Correlation effects were omitted in order to permit comparison with the RIA results. The first-order KMT optical potential was taken as[7]

$$U^{(1)}_{\rm NRIA}(r)=(2\pi)^{-3}\frac{A-1}{A}\sum_{j={\rm p,n}}\left[\int_0^\infty 4\pi q^2 dq\, t^a_{pj}(q)\tilde{\rho}_j(q)j_0(qr)+\frac{i\partial}{r\partial r}\int_0^\infty 4\pi q^2 dq\, \tilde{t}^c_{pj}(q)\tilde{\rho}_j(q)j_0(qr)\sigma\cdot l\right], \quad (33)$$

where

$$\tilde{t}^{c}_{pj}(q)=\frac{t^{c_0}_{pj}(q)}{\bar{k}^2_0\sin\theta_N}\ , \tag{34}$$

and θ_N is defined by $q=2\bar{k}_0\sin(\theta_N/2)$; q is the momentum transfer. The summation subscript j represents target protons and neutrons; the target density form factors, $\tilde{\rho}_j(q)$, were normalized such that $\tilde{\rho}_n(0)=N$ and $\tilde{\rho}_p(0)=Z$, where $N+Z=A$, the number of target nucleons.

The NN t matrices, t^a_{pj} and $t^{c_0}_{pj}$, in the pA Breit frame, were obtained from the matrix equation (applied separately for p-p and p-n)

$$\begin{bmatrix} t^a \\ t^b \\ t^{c_0} \\ t^{c_1} \\ t^d \\ t^e \end{bmatrix}_{s_{\rm Breit},t} = -\frac{4\pi(\hbar c)^2 E_{NN}}{E_p E_{SN}} B_A B_1^{-1} \begin{bmatrix} A \\ B \\ C \\ D \\ E \end{bmatrix}_{s_{\rm Breit},t}\ , \tag{35}$$

where the combined matrix operation $B_A B_1^{-1}$ accounts for relativistic spin precession effects; B_A and B_1 are given explicitly in Ref. 11. The $\{A,B,C,D,E\}$ are given in the impulse approximation (IA) by the NN c.m. scattering amplitudes defined in Eq. (14) at the kinematic values specified by $s_{\rm Breit}$ and t. The spin-orbit terms t^{c_0} and t^{c_1} apply to the projectile and target nucleon, respectively.[11] The kinematic quantities $\bar{k}_0$, E_p, and E_{SN} are the same as defined in Sec. II B. The total energy of either nucleon in the NN c.m. frame corresponding to $T_{\rm lab,eff}$(NN) appropriate to the specified momentum transfer q is denoted by E_{NN} in Eq. (35). Notice that the kinematic quantity $E_{NN}/(E_p E_{SN})$ is implicitly q dependent for the optimally factorized optical potential using Breit frame kinematics.

The same NN phase shifts (Arndt's SP82 solution) covering the same energy range, $T_{\rm lab}\rightarrow T_{\rm lab}+200$ MeV, were used to evaluate $U^{(1)}_{\rm NRIA}$ as in the RIA calculations. Also, the same ^{40}Ca, ^{48}Ca, and ^{208}Pb proton densities were used in evaluating $U^{(1)}_{\rm NRIA}$ as used for $\rho^p_V(r)$ in the RIA calculations. The neutron densities were obtained using Eq. (29) for the absolute NRIA predictions, whereas Eq. (30) provided $\rho_n(r)$ when fits to the differential cross section data were carried out. The Coulomb interaction was included according to the KMT No. 3 prescription discussed in Ref. 41. Electromagnetic spin-orbit effects were omitted in the NRIA calculations.

The first-order KMT optical potential was inserted in the radial Schrödinger equation with relativistic kinematics,[7]

$$\left\{\frac{d^2}{dr^2}-\frac{l(l+1)}{r^2}-\frac{2\mu_\epsilon}{\hbar^2}[U^{(1)\rm cen}_{\rm NRIA}(r)+U_{\rm Coul}(r)+U^{(1)\rm so}_{\rm NRIA}(r)\langle\sigma\cdot l\rangle_{lj}]+\bar{k}_0^2\right\}\psi_{lj}(r)=0\ , \tag{36}$$

where $\mu_\epsilon\equiv E_p E_A/(E_p+E_A)$ is the relativistic reduced energy, E_p (E_A) is the total energy of the incident proton (target nucleus) in the pA c.m. system, and

$$\langle\sigma\cdot l\rangle_{lj}=j(j+1)-l(l+1)-\tfrac{3}{4}$$

as usual. The central, spin-orbit, and Coulomb parts of the NRIA optical potential are shown explicitly in Eq. (36). The usual nonrelativistic scattering boundary conditions yielded the pA scattering amplitudes, which upon multiplication by $A/(A-1)$, led to the pA elastic observables.

IV. DISCUSSION AND RESULTS

Based on the various calculations performed in connection with this work it was found that variations in the overall matter or neutron density (with scalar-vector density differences fixed) primarily affected the angular positions of the diffractive minima and maxima in the differential cross sections ($d\sigma/d\Omega$), the analyzing power (A_y), the spin rotation (Q), and also the slope of the overall envelope encompassing $d\sigma/d\Omega$. Basic structures in the observables, such as the ratio of the maxima to adjacent minima in the angular distributions, the sharpness of diffractive minima, or the widths of the cross section maxima, the shapes of the minima and maxima in A_y and Q, overall magnitudes of the spin observables, etc., were not found to be affected by perturbations in the overall matter densities. Thus, to succinctly characterize the energy dependence inherent in both the RIA and NRIA models, the neutron vector and scalar densities were adjusted together to $|\chi|^2$ optimize the description of the differential cross section data. The energy dependence of these effective "neutron densities" will be discussed in the following.

In contrast to the gentle effects produced by small changes in the overall matter distributions, variations in the scalar-vector matter density difference produced significant changes in the structure of the computed analyzing power. Typical of these effects in A_y were alterations in the relative magnitudes of adjacent maxima, changes in the depths of the minima, gradual sharpening or smoothing of the first few maxima, and changes in the slope of the predicted A_y immediately following each maximum. The differential cross sections, however, were seen to be only very slightly affected by changes in the scalar densities; these changes were characterized by minimal variations in the magnitudes at angles beyond the Coulomb nuclear interference region and slight variation in the overall slope of the diffractive envelope. For these reasons, the energy dependences of the RIA analyzing power predictions will be summarized by examining the changes in the scalar-vector density difference (with fixed neutron-proton density differences) needed at each energy to optimize the RIA fit to the A_y data.

The reader is reminded of the fact that these energy

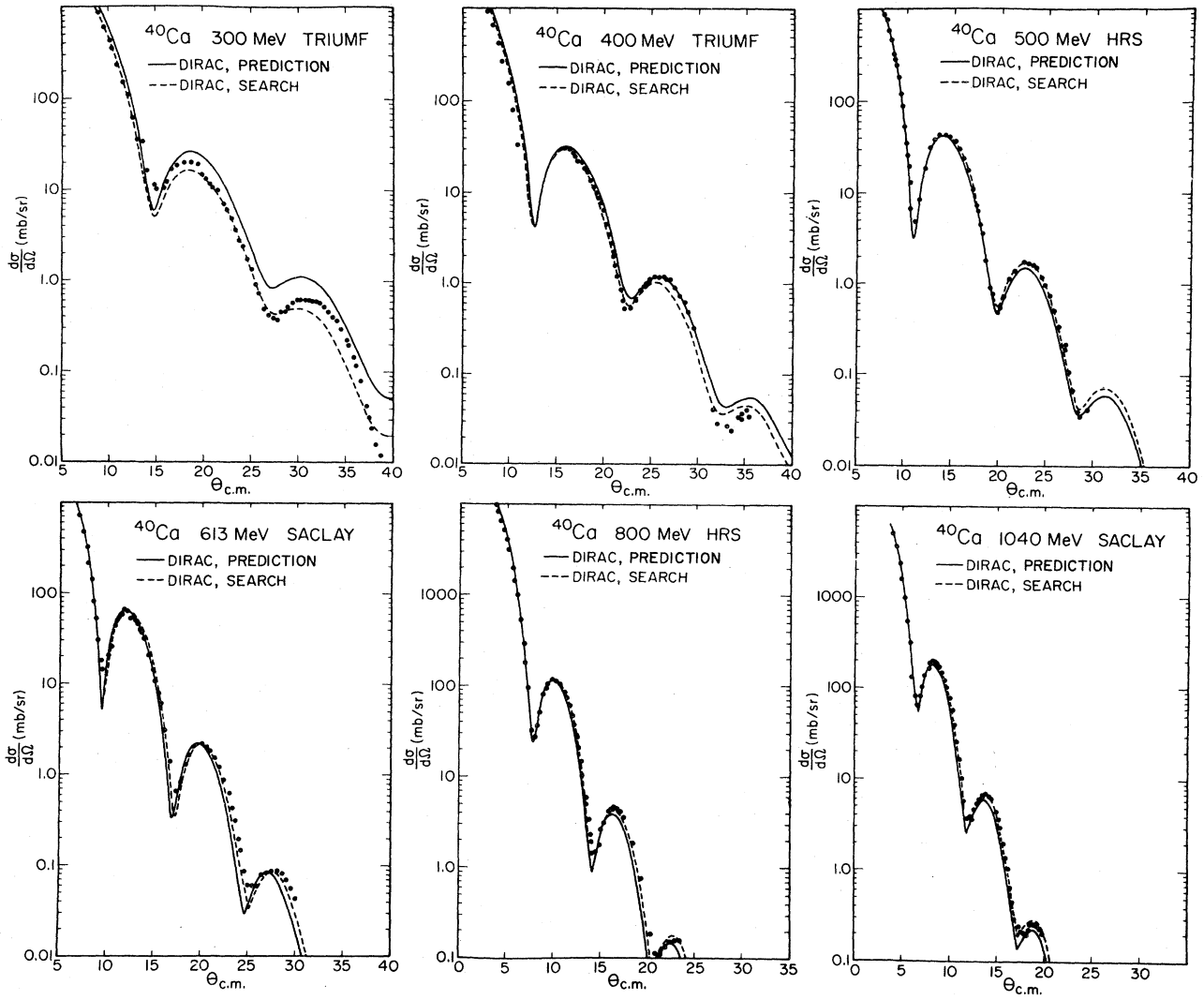

FIG. 4. p + ^{40}Ca RIA differential cross section predictions (solid curves) and fits (dashed curves) discussed in the text compared with data at 300, 400, 500, 613, 800, and 1040 MeV.

dependent, effective "densities," while reasonable in shape, are not intended to accurately represent the physical target densities. By requiring fits to the data, these effective densities absorb the contributions of reaction processes omitted in the calculations. The variation of the effective densities with energy directly indicates the magnitude of the effect which these omitted physical processes might have on extracted nuclear structure properties, such as the ground state neutron and scalar densities. In future work, when more sophisticated relativistic optical potentials are available which eliminate most of the large, erroneous energy dependences discussed here, simultaneous fits to the complete set of elastic observables should be carried out in which both the neutron-proton and scalar-vector density differences are varied.

A. Differential cross sections and sensitivity to neutron densities

The RIA and NRIA parameter free predictions for the 300, 400, 500, 613, 800, and 1040 MeV p + ^{40}Ca and the 300, 400, 500, 613, 800, and 1000 MeV p + ^{208}Pb elastic scattering differential cross sections are compared in Figs. 4–7 (solid curves) with the available data.[42] Generally the RIA predictions are too large in overall magnitude compared to the lower energy data, are quite good at 500 MeV, and are shifted inward in angle compared to the higher energy data. The RIA and NRIA fits to these data were optimized with respect to the total $|\chi|^2$ by adjusting the neutron densities discussed in Sec. II E. The results are shown by the dashed curves in Figs. 4–7. Good descriptions of the overall slope of the cross section envelope and angular positions of the diffractive maxima and minima are observed. However, the NRIA fits at the lower energies continue to display excessively deep diffractive minima, whereas the lower energy RIA fits exhibit diffractive patterns with relatively too little structure compared with the data. Even so, these results are quite informative with respect to the overall geometrical deficiencies of the predicted scalar and vector potentials in the RIA model and the central, spin-independent part of the NRIA optical potential.

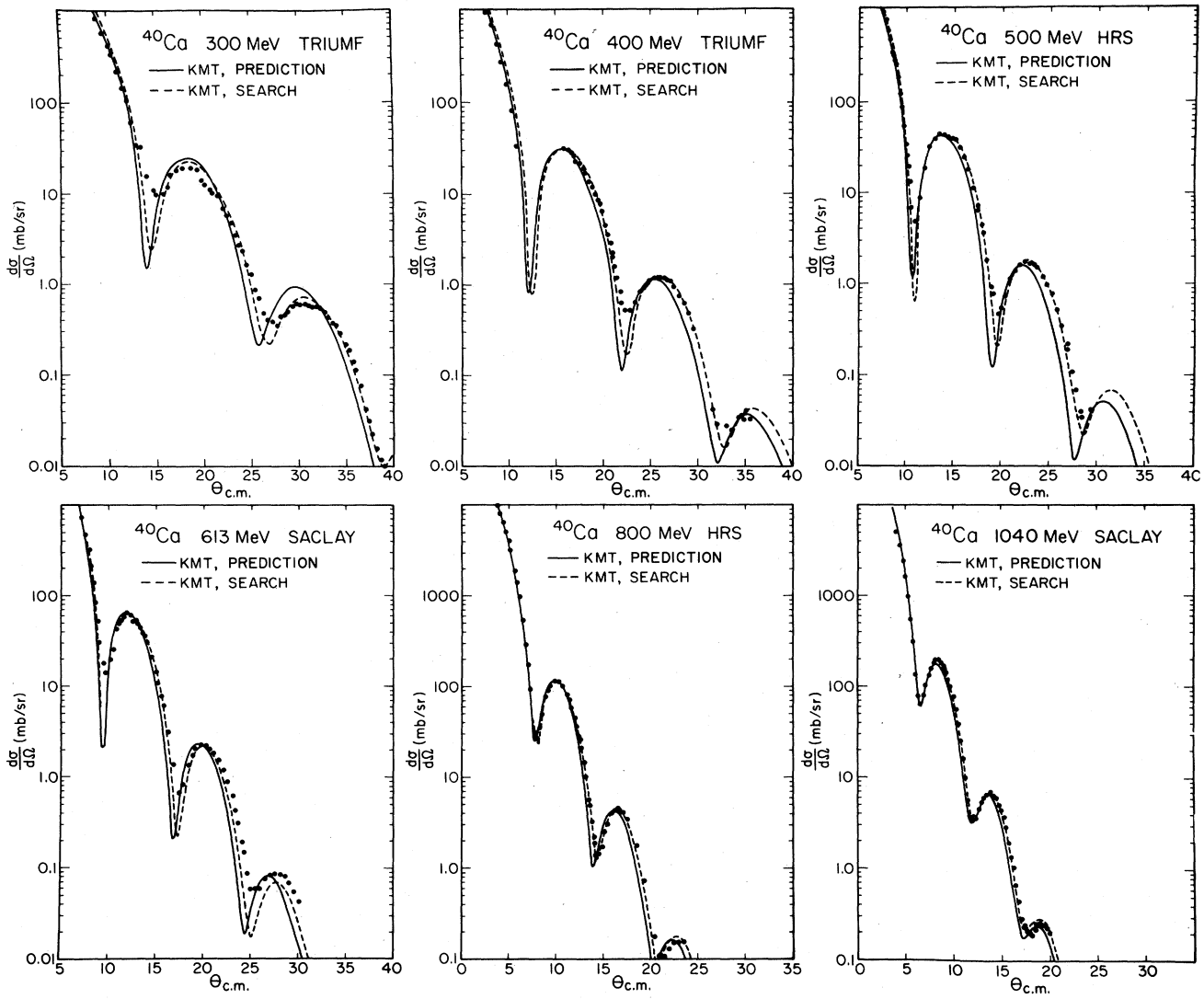

FIG. 5. Same as Fig. 4 except that NRIA predictions and fits are shown.

The information obtained from the $|\chi|^2$ fits is summarized in Figs. 8 and 9 for ^{40}Ca and Figs. 10 and 11 for ^{208}Pb; the theoretical predictions based on the HFB densities of Dechargé and Gogny[39] are also shown. Figures 8 and 10 display the deduced neutron-proton root mean square (rms) radius difference (neutron and proton vector density rms radii are used for the RIA results) as a function of incident proton energy. The NRIA results show a rather smooth energy dependence, underpredicting the expected absolute magnitude of the neutron rms radius at all energies, but gradually approaching the theoretical value as the incident energy increases. The RIA results, on the other hand, show a more radical energy dependence, with large overpredictions of the neutron rms radius obtained at lower energies and underestimates at higher energies. The success of the RIA at 500 MeV (Refs. 17 and 18) is seen in light of this result to be merely fortuitous with respect to the differential cross section predictions. Again, at the higher energies the RIA and NRIA results seem to be converging and approaching the theoretical values of the neutron rms radius. It is expected that the differences between the RIA and NRIA differential cross section predictions will diminish with increasing proton energy, since the increased absorption and the reduced spin-orbit coupling[21] both result in a quenching of the virtual pair contribution.

Similar energy dependences are observed in Figs. 9 and 11 for the parameters of the fitted neutron density radius and diffuseness. Shown are the ratios c/c_{STD} and z/z_{STD} [see Sec. II E and Eq. (30)] obtained for ^{40}Ca and ^{208}Pb at each energy studied. The RIA approach again gives evidence of a stronger energy dependence for the diffuseness parameter than does the NRIA (see the upper portions of Figs. 9 and 11). As the energy increases, the relativistic and nonrelativistic results for z/z_{STD} appear to converge, although not necessarily to the theoretical value. The lower portions of Figs. 9 and 11 show similar trends for the energy variations of the effective neutron radius pa-

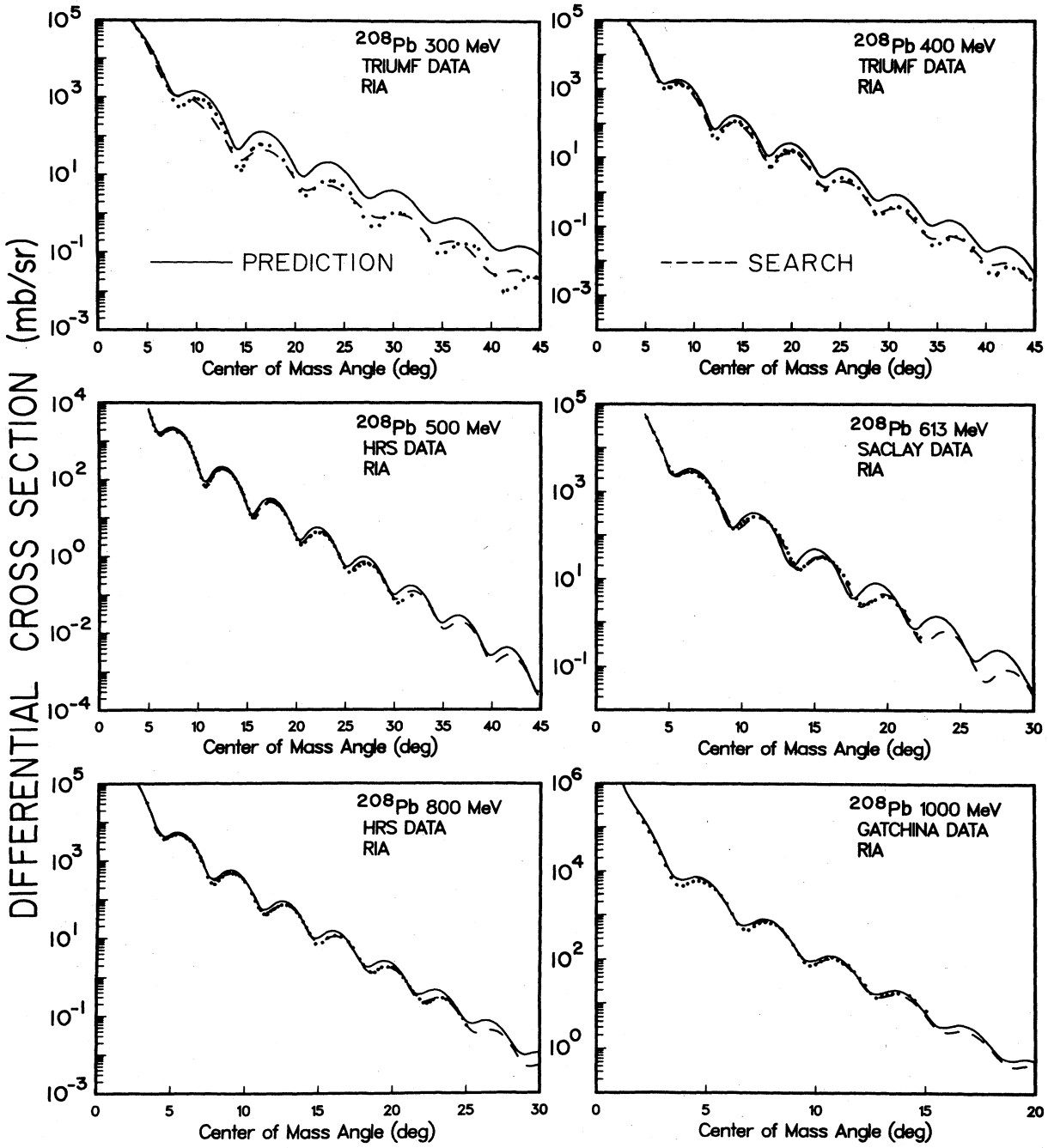

FIG. 6. p + ^{208}Pb RIA differential cross section predictions (solid curves) and fits (dashed curves) discussed in the text compared with data at 300, 400, 500, 613, 800, and 1000 MeV.

rameter. The convergence of the relativistic and nonrelativistic results at the higher energies is apparent for ^{208}Pb, but uncertain for ^{40}Ca. For the energy range investigated here, it does not appear that the extracted neutron half-density radii approach the theoretical values. This suggests that additional corrections to the simple impulse approximation are required at all energies.

Of particular interest in Figs. 8–11 is the anomalous behavior of the density results obtained from analysis of the 613 MeV data. Both the RIA and NRIA energy dependences of the extracted rms radii for ^{40}Ca and ^{208}Pb abruptly change as the proton energy increases above 600 MeV. Furthermore, the extracted neutron half-radius and, to a lesser extent, the diffuseness parameters, display departures from the otherwise smooth energy dependences observed. Analyses of preliminary p + ^{40}Ca 650 MeV

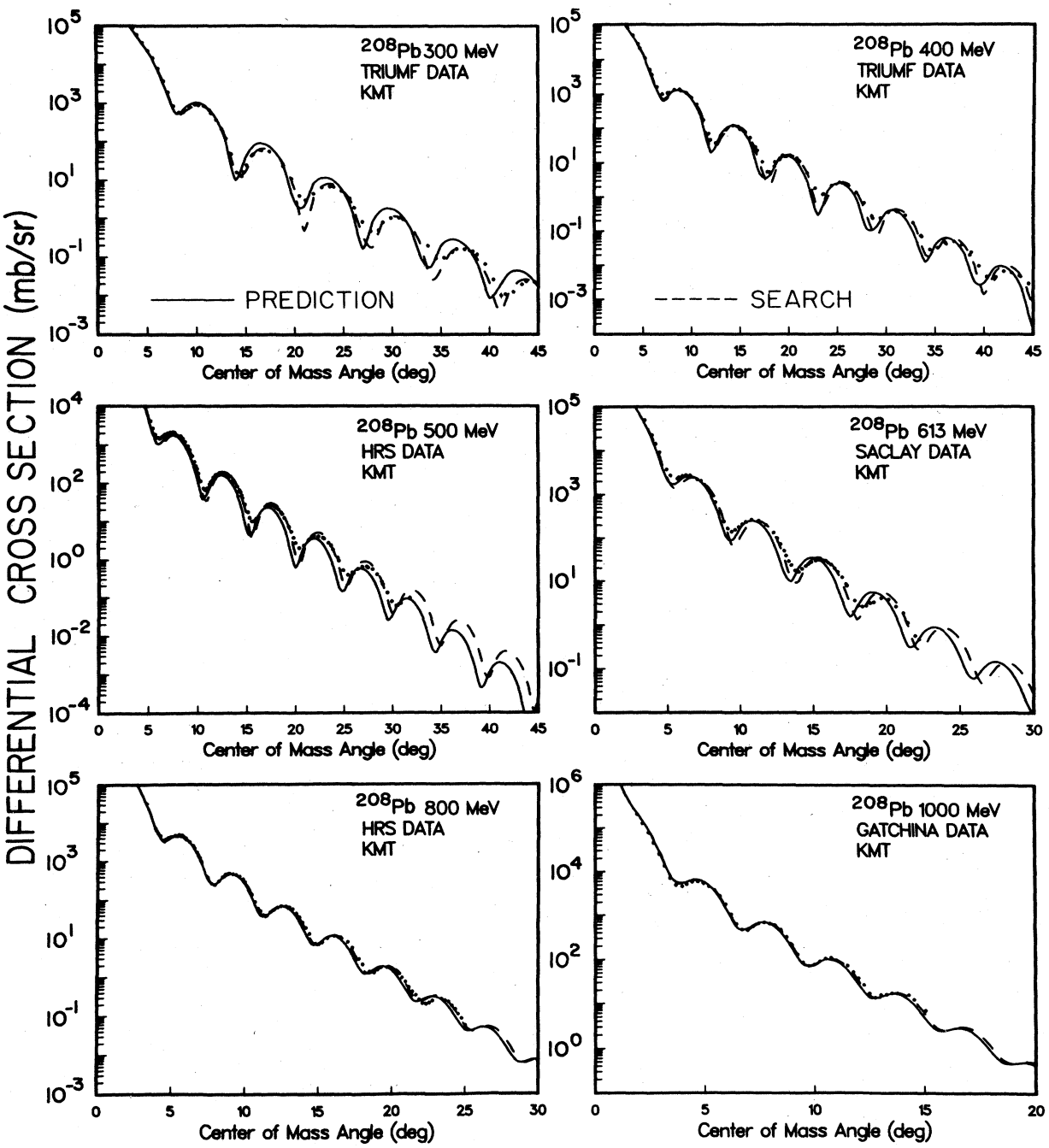

FIG. 7. Same as Fig. 6, except that NRIA predictions and fits are shown.

LAMPF—high-resolution spectrometer (HRS) data[43] give similar results. The NN amplitudes which affect these results should be uniformly reliable from 500—800 MeV, based on the roughly even distribution of NN data throughout this energy region.[21] Further analyses and perhaps more, high quality pA data in this energy region are required to determine whether these observations are consequences of new reaction mechanisms which are primarily operative in the 600 MeV region or of deficiencies in both models which become important at energies below 600 MeV. A discussion of probable theoretical deficiencies in the RIA model with respect to the energy dependence trends will be given in the last part of this section.

Another, particularly sensitive measure of the accuracy of the pA microscopic optical potentials is the ability of the models to provide consistent, energy independent neutron isotopic density differences. The RIA and NRIA models were therefore used to analyze the p + ^{48}Ca differential cross section data at 500 and 800 MeV.[42] The data were fit in the manner already discussed; the results

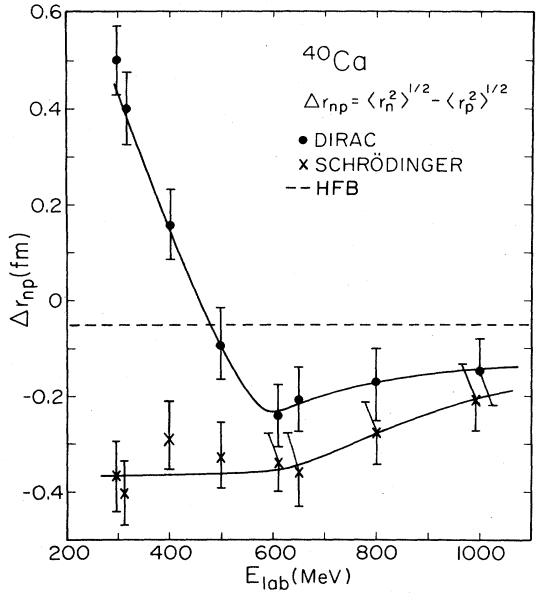

FIG. 8. Neutron-proton density rms radii differences for ^{40}Ca deduced using the RIA (solid dots) and the first-order NRIA (crosses). The uncertainties of ±0.07 fm reflect statistical and systematic uncertainties in the data, NN amplitudes, and fitting procedure (see Ref. 7). The theoretical value of −0.05 fm (Ref. 39) is indicated by the dashed line. The solid lines are guides to the eye. Points at 318 and 650 MeV result from analyses of preliminary HRS data.

are given in Figs. 12 and 13 and Table I. At 500 MeV the NRIA fits are poor (dash-dot curves) near the diffractive minima so that interpretation of the NRIA 500 MeV neutron density difference should be viewed with some reservation. The fits for the remaining cases are good.

In Fig. 14(a) the NRIA ^{48}Ca−^{40}Ca neutron density differences obtained at 500 MeV (dash-dot curve) and 800

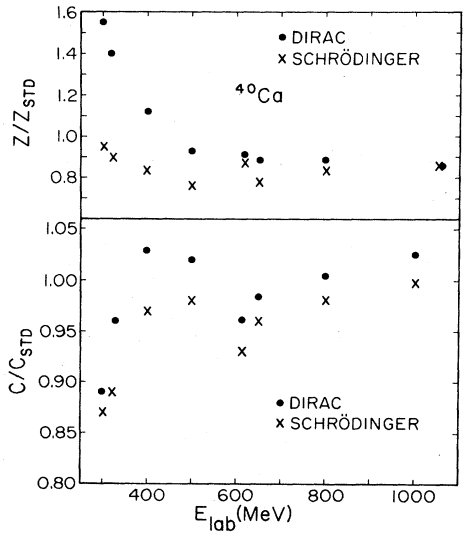

FIG. 9. Ratios of z/z_{STD} (upper portion) and c/c_{STD} (lower portion) needed in the RIA (solid dots) and NRIA (crosses) to fit the p + ^{40}Ca differential cross section data [see Eq. (30)].

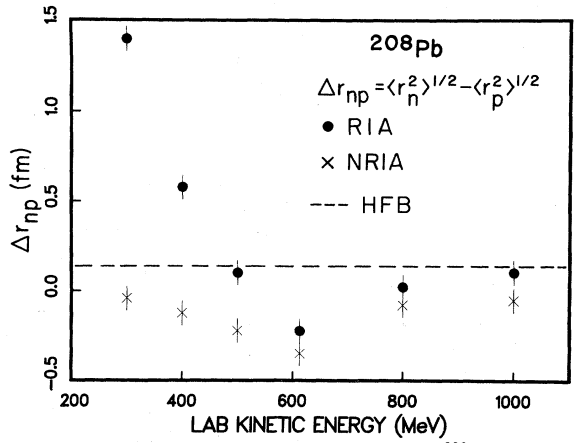

FIG. 10. Same as Fig. 8 except that the ^{208}Pb results are shown. The theoretical value of 0.13 fm (Ref. 39) is indicated by the dashed line.

MeV (solid curve) are compared. The differences between the two curves are comparable to or less than the statistical and model dependence uncertainties arising in careful, second-order KMT-IA analyses[44] of the 800 MeV data and indicate the stability of isotopic density differences obtained with NRIA models. The corresponding RIA neutron-vector density differences are shown in Fig. 14(b) where a larger energy variation is noted. In the Schrödinger equivalent optical potential approach to the RIA (Ref. 15), isotopic density differences (linear density

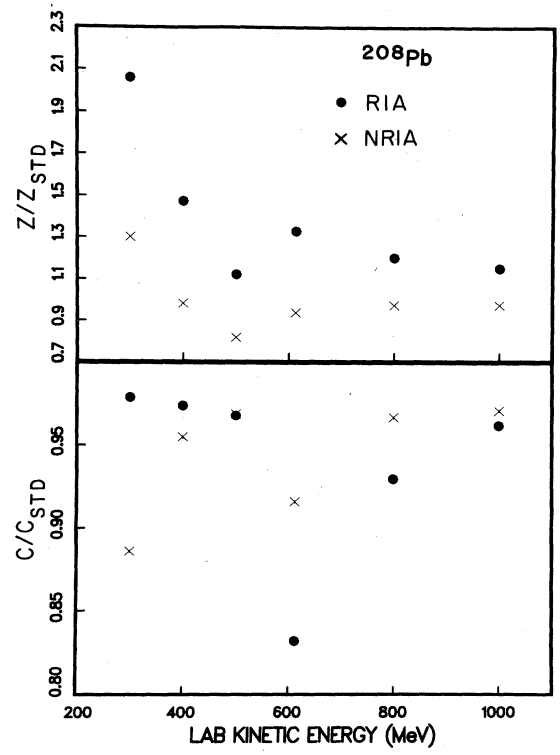

FIG. 11. Same as Fig. 9 except these indicate the ^{208}Pb results.

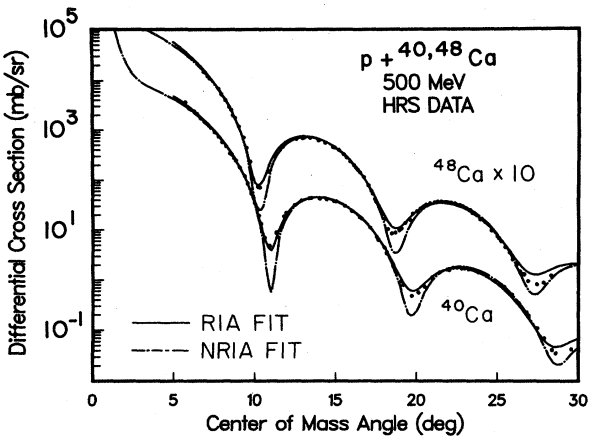

FIG. 12. RIA (solid curves) and NRIA (dash-dot curves) fits to the p + ^{40}Ca and ^{48}Ca HRS differential cross section data at 500 MeV.

differences) are affected directly by nonlinear density dependent components in the Schrödinger equivalent optical potential. Thus, Fig. 14(b) may indicate an inadequacy in the treatment of the virtual pair terms in the RIA. A number of corrections to the RIA, including medium modifications, correlations, and off-shell dependences, could combine with the virtual pair process to alter the overall nonlinear density-dependent components of the Schrödinger equivalent form of the RIA optical potential. This point will be discussed further in Sec. IV C.

Finally, the RIA (solid curve) and NRIA (dash-dot curve) results for the 800 MeV ^{48}Ca−^{40}Ca neutron density difference are compared directly in Fig. 14(c). The virtual pair effects in the RIA approach cause the differences between the two curves. Again, the difference between the RIA and NRIA isotopic density differences is comparable to the uncertainties in the results of second-order KMT analyses. Since the 800 MeV second-order KMT-IA model has been shown to give accurate matter density differences in this mass regime,[45] and owing to the apparent energy dependence for extracted isotopic density

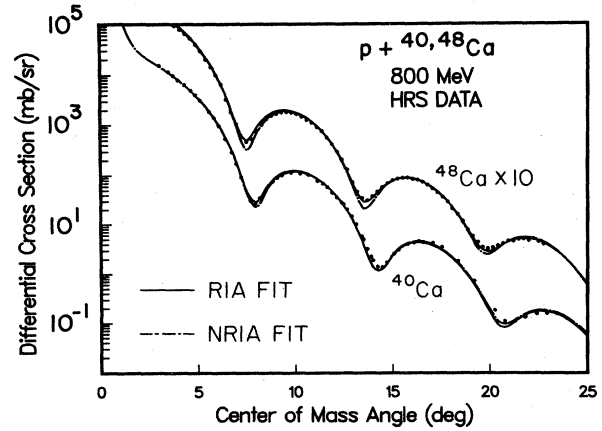

FIG. 13. Same as Fig. 12, except at 800 MeV.

TABLE I. Extracted neutron rms radii (in fm).

	500 MeV	800 MeV	Theory (HFB)
		Δr_{np} NRIA	
^{40}Ca	−0.34	−0.27	−0.045
^{48}Ca	−0.14	−0.11	0.13
		Δr_{np} RIA	
^{40}Ca	−0.03	−0.15	−0.045
^{48}Ca	0.13	−0.02	0.13
		$\Delta r_{nn'}$ (^{48}Ca−^{40}Ca)[a]	
	NRIA	RIA	Theory (HFB)
500 MeV	0.21±0.05	0.18	0.20
800 MeV	0.18±0.05	0.14	0.20

[a]Second order KMT-IA analysis at 800 MeV yields $\Delta r_{nn'}=0.16\pm0.05$ fm, see Ref. 44.

differences obtained via the RIA model, the solid curve (RIA) in Fig. 14(c) should not necessarily be considered more representative of the true ^{48}Ca−^{40}Ca neutron density difference than the dash-dot curve (NRIA). The purpose of Fig. 14(c) is to demonstrate the kind of effects which the virtual pair processes in the RIA model produce in relative measurements of density variations in neighboring nuclei. Notice that although the ^{48}Ca−^{40}Ca density distribution differences for the RIA display greater energy dependence than do the NRIA differences, the energy dependence of

$$\Delta r_{nn'}=\langle r_n^2(^{48}\mathrm{Ca})\rangle^{1/2}-\langle r_n^2(^{40}\mathrm{Ca})\rangle^{1/2}$$

is modest and comparable for the two models (see Table I). All of the extracted values of $\Delta r_{nn'}$ are in fair agreement with the HFB predictions.[39]

B. Analyzing power, spin rotation, and sensitivity to scalar densities

The RIA and NRIA parameter-free predictions for the p + ^{40}Ca elastic analyzing power A_y at 300, 400, 500, 800, and 1000 MeV are shown together with the data[42] in Fig. 15 by the solid and dash-dot curves, respectively. Similarly, the results for p + ^{208}Pb at these same energies are given in Fig. 16. The spin-rotation $Q(\theta)$ predictions for p + ^{40}Ca and ^{208}Pb at 500 MeV are shown in Fig. 17 by the solid (RIA) and dash-dot (NRIA) lines. In Fig. 15, shown as the dashed curves, are the fits obtained by varying the scalar density (see the following). The effects of the anomalous magnetic moment of the incoming proton in the RIA model [see Eq. (28)] and the electromagnetic spin-orbit (EMSO) coupling in the NRIA approach[12] were omitted in the absolute predictions shown in Figs. 15–17. Such magnetic effects are only appreciable at and above 800 MeV (Refs. 6 and 12); they affect the position of the first maximum in A_y and the sharpness of the forward angle analyzing power diffractive structure. Inclusion of the EMSO coupling in the NRIA approach requires a difficult series of convergence calculations to be carried out for each case.[12] Since our main intent is to provide a relative comparison between results from relativistic and cor-

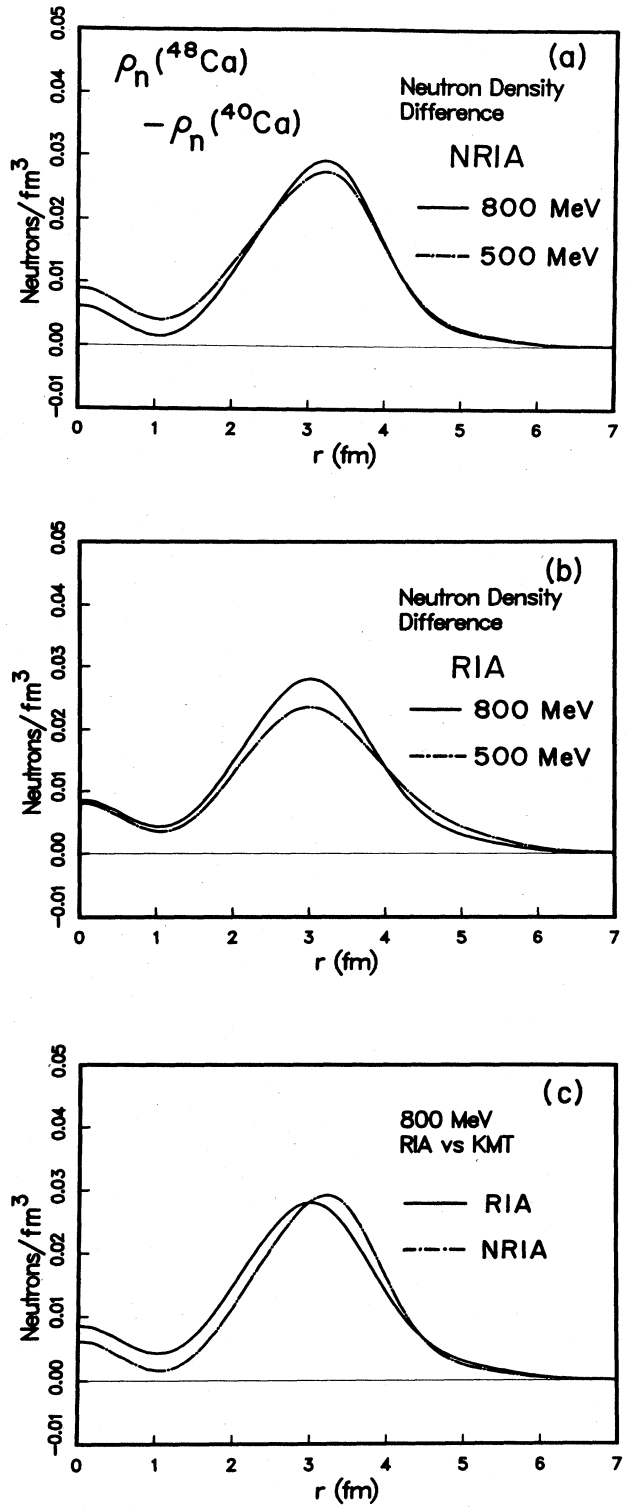

FIG. 14. (a) $^{48}Ca-^{40}Ca$ neutron density differences obtained at 800 MeV (solid line) and 500 MeV (dash-dot line) using the NRIA model. (b) Same as (a) except the RIA model results are shown. (c) Comparison of the $^{48}Ca-^{40}Ca$ neutron density differences obtained at 800 MeV using the RIA (solid curve) and NRIA (dash-dot curve).

responding nonrelativistic models, this effect was omitted for simplicity. However, for the RIA fits to the A_y data in which the scalar densities were varied (discussed in the following), the anomalous magnetic moment effects were included.

The noteworthy features of the parameter-free predictions in Figs. 15–17 are the following: (1) the lack of structure at forward angles for the NRIA A_y results (dash-dot lines), (2) the generally successful large angle NRIA A_y results for ^{40}Ca, (3) the overestimate of the NRIA A_y results at back angles for ^{208}Pb (i.e., the NRIA suffers an incorrect mass dependence with respect to the spin components of the effective interaction), (4) the underestimate of the magnitude and the incorrect mass dependence of the NRIA results for Q, (5) the generally favorable results for the RIA A_y as a function of energy, mass, and scattering angle, and (6) the good reproduction of Q provided by the RIA. The good description of the available spin-rotation data[42,46] obtained with the RIA is perhaps the strongest asset of the model. The RIA predictions for Q are in fact remarkably stable. Gross, factor of 2, changes in the underlying NN amplitudes which have large effects on the cross section and analyzing power predictions leave the essential structure of Q unchanged.

Earlier it was noted that the analyzing power predictions are particularly sensitive to scalar-vector density differences. In Figs. 18–20 various A_y, Q, and S (Ref. 47) predictions are compared for $p+^{40}Ca$ at 300, 500, and 800 MeV, respectively. They were obtained using the RIA (solid curve), NRIA (dash-dot curve), and RIA with $\rho_S^{(i)}=\rho_V^{(i)}$ (dashed curves) (i.e., no lower components of the target wave function permitted). The differences between the solid and dashed lines reveal the effects of relativity in the target wave function, while comparison of the dashed and dash-dot curves indicates the role of relativity (virtual pair processes) in describing the projectile proton wave function. At 300 MeV relativistic target effects are comparable to relativistic projectile effects, while at higher energies the virtual pair terms for the projectile mainly account for the differences between RIA and NRIA results and the improvements in the descriptions of the pA spin observable data. Note that the relativistic effects are very evident for the alternate (not independent) spin observable, S (Ref. 47), at 300 MeV.

The sensitivity of the RIA A_y predictions to the scalar-vector density difference, was exploited by varying the proton and neutron scalar densities for ^{40}Ca, as discussed in Sec. II E, to minimize the total $|\chi|^2$ of the fit to the A_y data. The results (see dashed curves of Fig. 15) demonstrated main sensitivity to the scaling parameter ξ in Eq. (32); little sensitivity to the radial parameter $\bar{R}$ was found. Generally, the description of the analyzing power data was improved at all angles by variation of ξ and $\bar{R}$, except at 400 MeV where the fits in the mid and back angle regions were improved at the expense of the forward angle fits. The energy dependence of the scale factor ξ is displayed in Fig. 21. $\xi=1.0$ corresponds to the target wave function lower component strength of Horowitz and Serot. The point at 650 MeV results from an analysis of preliminary $p+^{40}Ca$ A_y data provided by Bernstein and

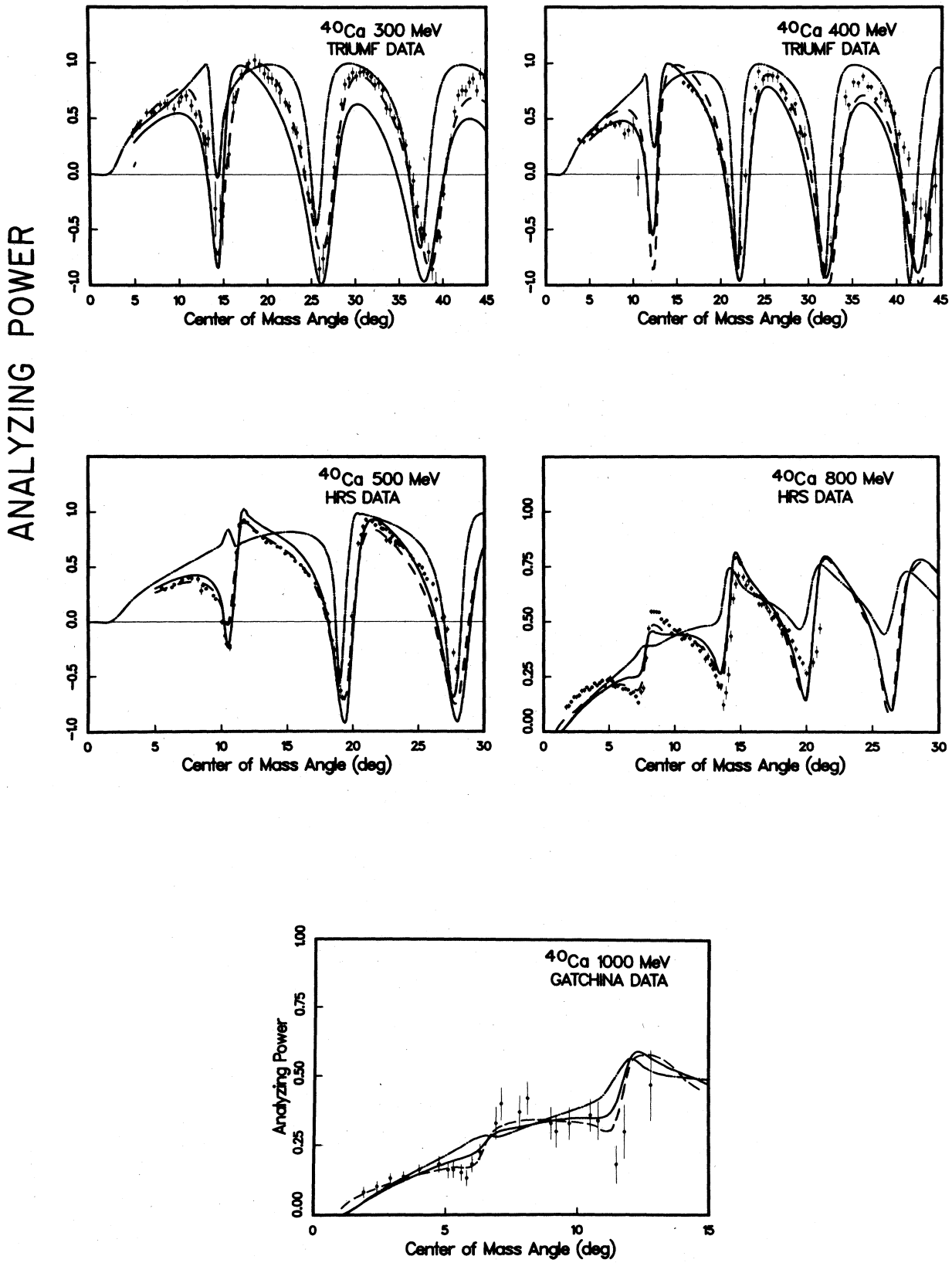

FIG. 15. $p + {}^{40}Ca$ analyzing power RIA predictions (solid curves), NRIA predictions (dash-dot curves), and RIA fits (dashed curves) compared with data at 300, 400, 500, 800, and 1000 MeV as discussed in the text.

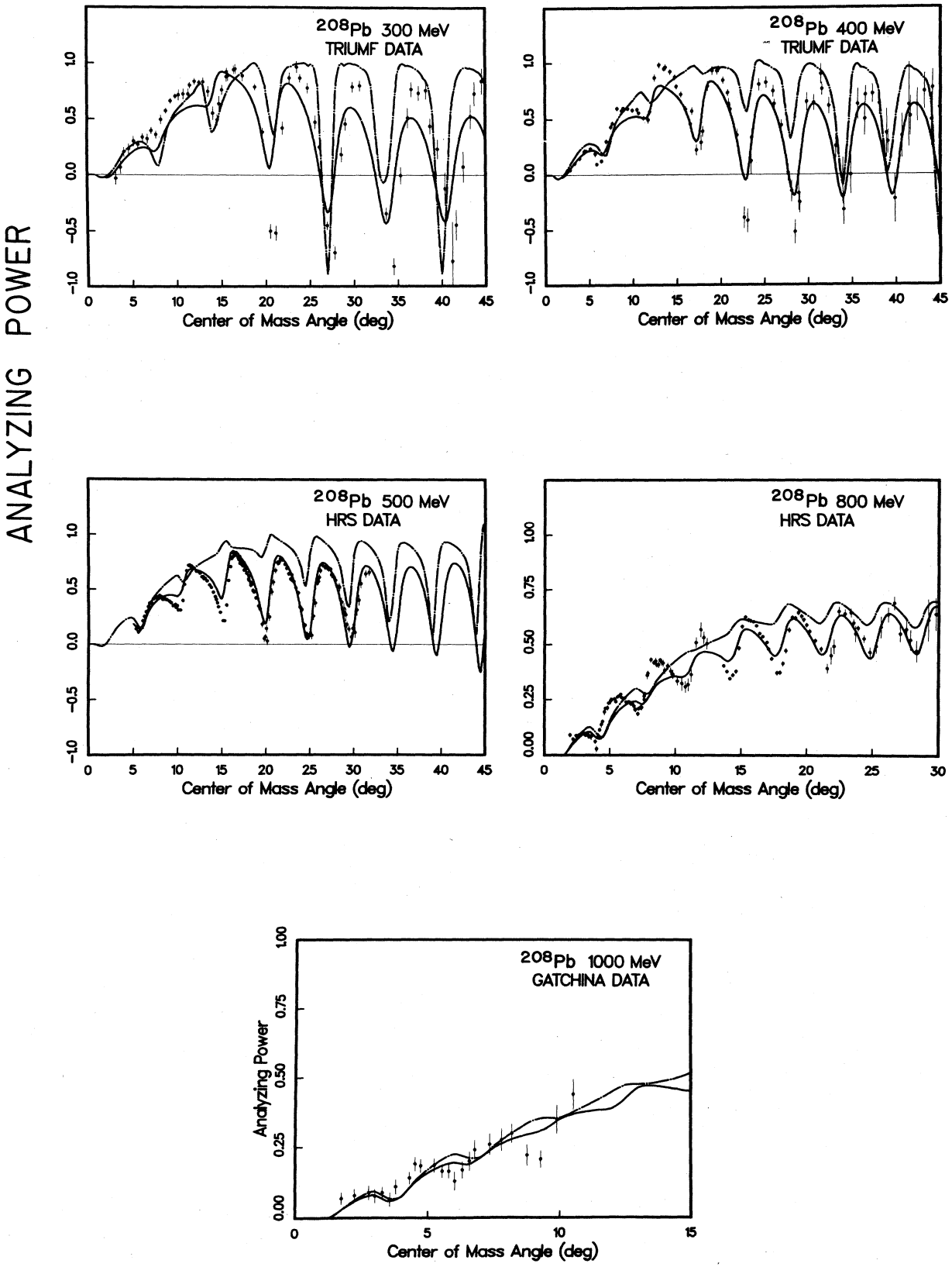

FIG. 16. p + ^{208}Pb analyzing power RIA (solid curves) and NRIA (dash-dot curves) predictions compared with data at 300, 400, 500, 800, and 1000 MeV as discussed in the text.

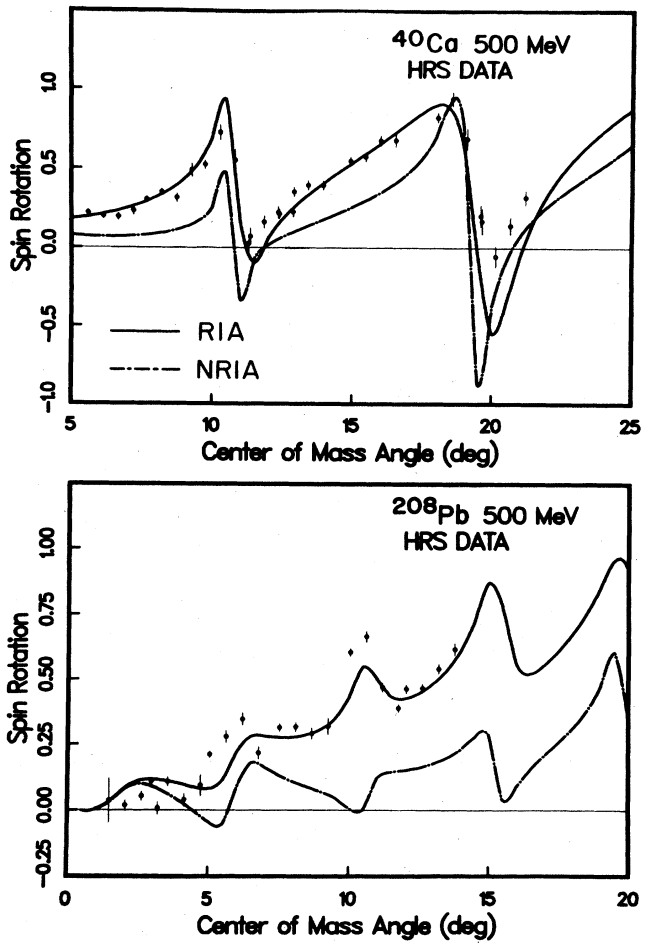

FIG. 17. RIA (solid curves) and NRIA (dash-dot curves) predictions for 500 MeV p + ^{40}Ca and ^{208}Pb spin-rotation functions in comparison with data.

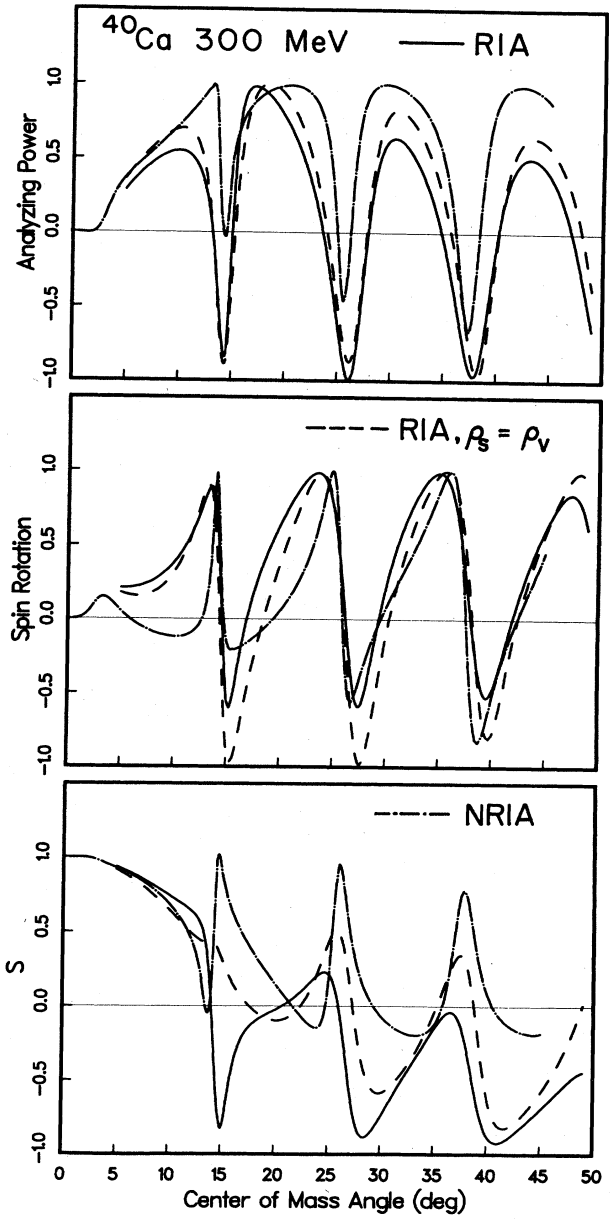

FIG. 18. RIA (solid curves), RIA with $\rho_S = \rho_V$ (dashed curves), and NRIA (dash-dot curves) predictions for p + ^{40}Ca analyzing power (upper portion), spin rotation (middle portion), and S (lower portion) at 300 MeV.

Miskimen.[48] This exercise demonstrates the considerable sensitivity of the RIA spin-dependent observables to the lower components of the target wave function as well as some further energy dependent characteristics. The present relativistic model is too simple to permit meaningful studies of the actual scalar densities of ^{40}Ca and ^{208}Pb to be undertaken.

C. Further theoretical improvements needed in relativistic optical models

Discussion of the trends summarized in Figs. 8—11, 14, and 21 is readily divided into three different categories corresponding to three energy domains. First, below 400 MeV, a serious, though not unexpected, breakdown of the RIA, and the NRIA to a lesser extent, is apparent. Second, the results suggest a departure near 600 MeV from the otherwise smooth energy dependent trends observed for both the RIA and NRIA. Finally, an asymptotic region above 800 MeV is manifest where both models give results that converge towards each other and where the energy variations are slight.

It is not surprising that both impulse approximation models are inadequate at lower energies ($T_{\text{lab}} \leq 400$ MeV); Pauli blocking, binding energy, target nucleon correlations, and an explicitly nonlocal treatment of NN exchange are each expected to play a greater role owing both to the reduced NN relative momentum and the increased NN effective interaction strength. Pauli blocking effects have been estimated by Horowitz[25] to be significant for the low energy relativistic optical potential, but above 500 MeV they are expected to be small based on preliminary

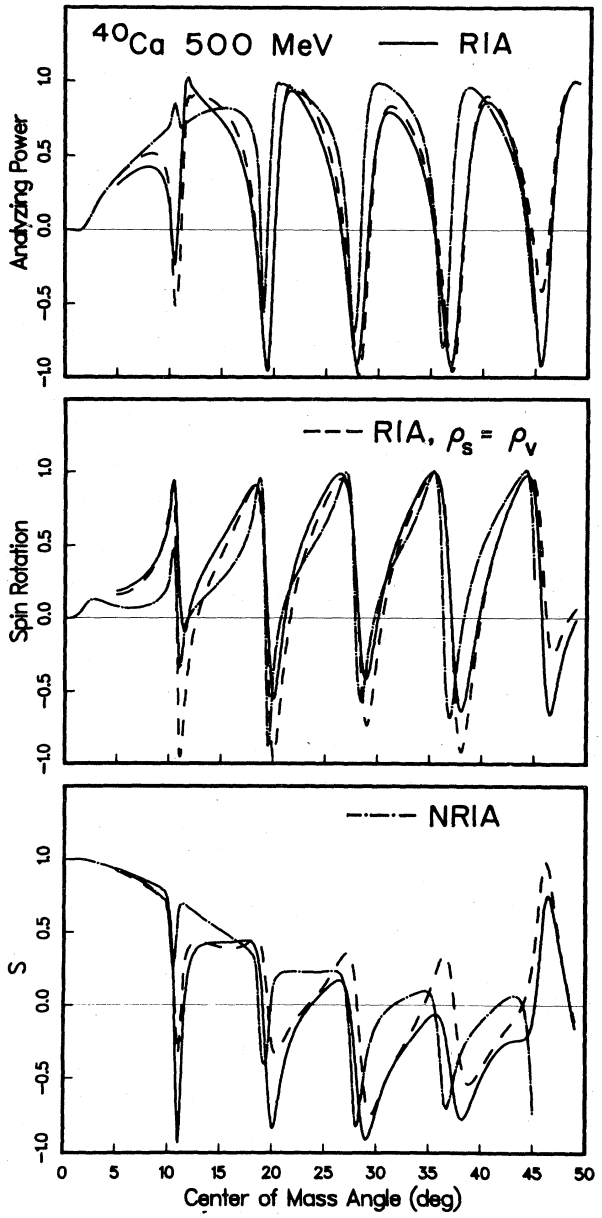

FIG. 19. Same as Fig. 18, except for 500 MeV.

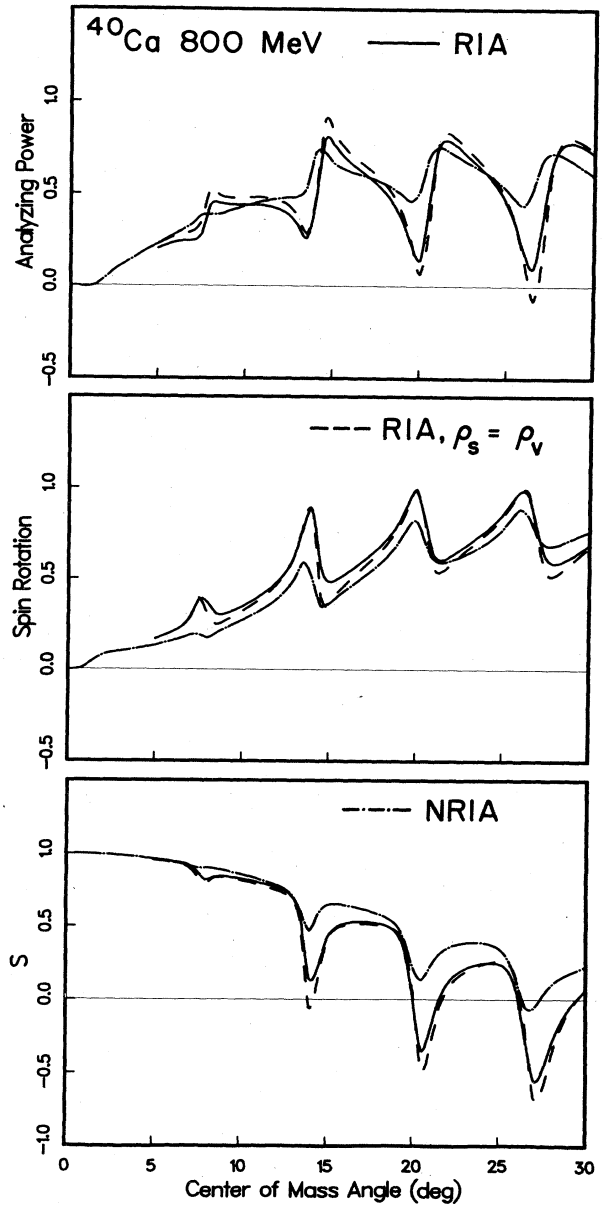

FIG. 20. Same as Fig. 18, except for 800 MeV.

estimates using a nonrelativistic isobar coupled-channel approach.[14]

Corrections to the pA optical potential due to target nucleon correlations[2] have been investigated in nonrelativistic (NR) microscopic optical model theories;[6,7] significant contributions to the differential cross sections and analyzing power were observed, particularly at the higher energies where the NR potential is strongest. These corrections are ρ^2 in form and in the relativistic optical model might also produce significant effects similar to the virtual pair processes. Recent work by Wallace and Tjon[24] suggests, however, that much of the unacceptable energy dependence exhibited by the RIA model below 500 MeV might be eliminated if the virtual pair process [i.e., the second term of U_{eff}^{++} in Appendix A, Eq. (A3)] is computed by way of a covariant meson exchange theory of the NN interaction.[23]

The results presented in this section suggest an interesting energy dependent structure around 600 MeV. If this trend persists after the preceding corrections are considered, one might also consider virtual Δ production and propagation,[49] since $\simeq$600 MeV coincides with the laboratory energy for NN resonance Δ production.

It is important to note that deficiencies remain in the RIA and NRIA models; even at 1 GeV. Medium effects should be minimal at these higher energies. Also the quenched virtual pair effects (i.e., the reduction in the RIA-NRIA differences) at higher energies suggest that a

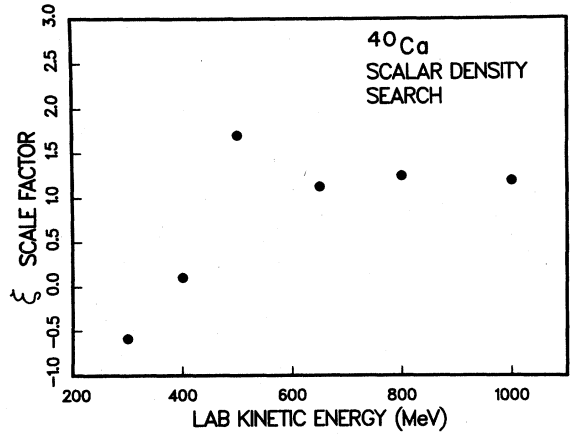

FIG. 21. Scaling factor, ξ [see Eq. (32)], for the overall strength of the scalar-vector density difference obtained in the RIA fits to p + ^{40}Ca analyzing power data at 300, 400, 500, 650 (Ref. 48), 800, and 1000 MeV.

more sophisticated treatment of this relativistic reaction mechanism is unnecessary. Target correlation effects, known to be significant at 1 GeV from NR optical model work,[6,7] also need to be included in the RIA. For instance, the vector and scalar densities deduced from RIA fits to the higher energy data, as well as the energy dependence in the extracted neutron isotopic density difference obtained in the RIA analysis, could be significantly affected by correlation terms.

V. CONCLUSIONS

We have focused on systematic energy dependent characteristics of the relativistic impulse-approximation—Dirac-equation approach for intermediate energy proton-nucleus elastic scattering. The observed characteristics were compared with those obtained from the traditional nonrelativistic impulse-approximation—Schrödinger-equation method. The energy dependence was explicitly displayed by comparing the predictions for the elastic observables directly with data and indirectly, but more succinctly, by examining the effective density parameters required to fit the differential cross section and A_y data at each energy.

With respect to the differential cross sections, the RIA model gave evidence of a more extreme energy variation relative to the data than did the NRIA model, particularly at low energies. However, above 500 MeV, where medium modifications and off-shell effects should be less important, the RIA analysis yielded effective neutron rms radii (for ^{40}Ca and ^{208}Pb) and neutron surface geometries (mainly for ^{40}Ca) which are closer to theoretical expectations than those obtained from the NRIA analysis. It was also shown that the effect of the relativistic virtual pair process, exemplified by the differences between the corresponding RIA and NRIA predictions, diminishes with increasing proton bombarding energy. This results from increased absorption, which depletes the proton distorted wave function in the high density regions of the nucleus, and reduced spin-orbit coupling, which lessens the magnitudes of the ρ^2 terms in the NR Schrödinger equivalent optical potential.[15] Through this study we also demonstrated the sensitivity of the RIA optical model analysis to the underlying neutron densities; we found sensitivities similar to those seen in KMT-IA optical model analyses. The variations with energy of the deduced effective densities reflected the magnitude of the perturbation in the extracted nuclear structure properties which further theoretical corrections will likely produce.

The generally successful description of the analyzing power data via the RIA model, originally noted at 500 MeV,[17,18] was shown to be a general feature of the relativistic description. The structure of the A_y predictions was seen to be acutely sensitive to the scalar-vector density difference (i.e., lower components of the relativistic target wave functions) and an interesting energy dependence for the overall scalar-vector density strength was observed.

The RIA fits to the spin-rotation (Q) data were particularly successful. Calculations in which gross (factor of 2) changes were made in the strengths of the NN amplitudes, along with the density variations discussed in Sec. IV, demonstrated the remarkable stability of the RIA model predictions for Q.

The results obtained here for the energy dependent systematics of the RIA and NRIA optical potential models will hopefully serve as a guide in future theoretical improvement in these impulse models.

ACKNOWLEDGMENTS

The authors would like to thank Dr. B. C. Clark, Dr. S. Hama, Dr. C. J. Horowitz, Dr. P. C. Tandy, Dr. R. M. Thaler, and Dr. S. J. Wallace for several useful discussions concerning this work. Thanks are also expressed to Dr. E. D. Cooper for providing a Dirac equation computer code used in portions of this research. We also thank Dr. D. A. Hutcheon for permission to show some of the unpublished TRIUMF elastic scattering data, and Dr. A. Bernstein and Dr. R. Miskimen for making available the preliminary p + ^{40}Ca 650 MeV A_y data. This research was supported in part by the Robert A. Welch Foundation and the U. S. Department of Energy.

APPENDIX A

In Sec. II C it was noted that pA elastic scattering predictions can be affected by terms contributing to $\hat{F}$ in Eq. (15) which project out of the positive energy matrix elements formed in Eq. (16). To make this point transparent we introduce the usual positive and negative energy projection operators Λ_+ and Λ_- (Ref. 28). Equation (6) in the text then becomes[33]

$$\begin{aligned} T_{00}^{++} &= U_{\rm opt}^{++} + U_{\rm opt}^{++} G^+ T_{00}^{++} + U_{\rm opt}^{+-} G^- T_{00}^{-+} , \\ T_{00}^{-+} &= U_{\rm opt}^{-+} + U_{\rm opt}^{-+} G^+ T_{00}^{++} + U_{\rm opt}^{--} G^- T_{00}^{-+} , \end{aligned} \tag{A1}$$

where $T_{00}^{\pm\pm} \equiv \Lambda_\pm PTP\Lambda_\pm$, $U_{\rm opt}^{\pm\pm} \equiv \Lambda_\pm U_{\rm opt}\Lambda_\pm$, $G^+ \equiv \Lambda_+ PGP\Lambda_+$ propagates positive energy projectile states, and $G^- \equiv \Lambda_- PGP\Lambda_-$ propagates negative energy states. $U_{\rm opt}$ is given either by Eq. (7) or (9) in the text. Eliminating T_{00}^{-+} in Eq. (A1) gives

$$T_{00}^{++}=U_{\rm eff}^{++}+U_{\rm eff}^{++}G^{+}T_{00}^{++}\ , \tag{A2}$$

where

$$U_{\rm eff}^{++}=U_{\rm opt}^{++}+U_{\rm opt}^{+-}\frac{1}{(G^{-})^{-1}-U_{\rm opt}^{--}}U_{\rm opt}^{-+}\ . \tag{A3}$$

For example, it is clear from Eqs. (A2) and (A3) that components of $\hat{F}$ which contribute to $(\bar{u}'_1\bar{u}'_2\hat{F}v_1u_2)$ matrix elements (u and v represent positive and negative energy Dirac spinors, respectively), but not to the positive energy matrix element $(\bar{u}'_1\bar{u}'_2\hat{F}u_1u_2)$, can contribute to pA scattering observables through the second term in Eq. (A3).

APPENDIX B

The relationship between the invariant t matrix and the scattering amplitude for a general two-fermion scattering process, such as that shown in Fig. 22, can be obtained from the relativistic expression for the infinitesimal cross section. For arbitrary kinematics this is given by[28]

$$d\sigma=\int\frac{m_1m_2}{[(P_1\cdot P_2)^2-m_1^2m_2^2]^{1/2}}\,|\Upsilon|^2(2\pi)^4\delta^4(P'_1-P_1+P'_2-P_2)\frac{m_1d^3P'_1}{(2\pi)^3E'_1}\frac{m_2d^3P'_2}{(2\pi)^3E'_2}\ , \tag{B1}$$

which is in terms of the Lorentz invariant phase space, the incident flux, and the invariant t matrix, Υ. In Eq. (B1) m_1 and m_2 are the fermion masses; (E_1,E_2) and (E'_1,E'_2) are the initial and final total energies, respectively; (P_1,P_2) and (P'_1,P'_2) are the initial and final four momenta, respectively; and the delta function requires energy-momentum conservation. Identifying the scattering amplitude F as $d\sigma/d\Omega=|F|^2$, using Breit frame kinematics[11] where (1) refers to the incident particle and (2) to the struck particle, and following Bjorken and Drell,[28] we get

$$\Upsilon(s,t)=-\frac{2\pi(\hbar c)^2}{m_1m_2\sqrt{\bar{k}_0}}\left\{[(P_1\cdot P_2)^2-m_1^2m_2^2]^{1/2}\left[(E_{\rm p}+E_{\rm SN})-\frac{k_a^2}{\bar{k}_0^2}(1-1/A)E_{\rm p}\right]\right\}^{1/2}F(s,t)\ , \tag{B2}$$

where (s,t) are the usual Mandelstam invariants, $\bar{k}_0$ is the magnitude of the incident projectile momentum in the Breit frame, and $E_{\rm p}$, $E_{\rm SN}$, and k_a are defined in Sec. II B. In Eq. (B2) and throughout this Appendix the scattering amplitude, F, and t matrix, Υ, are assumed to have the one-column matrix structure introduced in Sec. II C. Evaluating Eq. (B2) for $m_1=m_2=m$ (the nucleon mass) yields for NN scattering,

$$\Upsilon(s,t)=-\frac{2\pi(\hbar c)^2}{m}R(q)F(s,t)\ , \tag{B3a}$$

where

$$R(q)=[E_{\rm p}^2E_{\rm SN}^2+2E_{\rm p}E_{\rm SN}(q^2/4+k_a^2/A)+q^4/16+q^2k_a^2/(2A)+k_a^4/A^2-m^4]^{1/4}\times\left[E_{\rm p}+E_{\rm SN}-\frac{k_a^2}{\bar{k}_0^2}(1-1/A)E_{\rm p}\right]^{1/2}\frac{1}{m\sqrt{\bar{k}_0}}\ . \tag{B3b}$$

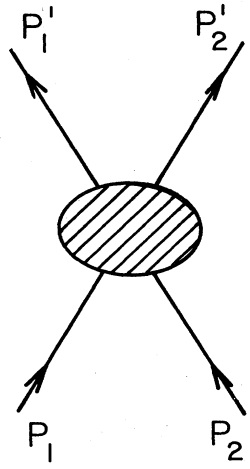

FIG. 22. Momenta and energies for the general two-body process, $1+2\rightarrow1'+2'$.

Equating the invariants $F_{\rm NN\,c.m.}/P_{\rm NN\,c.m.}$ and $F_{\rm NN,Breit}/\bar{k}_0$ (Ref. 49) yields [(NN c.m.) refers to the NN center-of-momentum system and (NN,Breit) to the Breit frame]

$$\Upsilon_{\rm Breit}(q)=-\frac{2\pi(\hbar c)^2}{m}R(q)\frac{\bar{k}_0}{P_{\rm NN\,c.m.}}F_{\rm NN\,c.m.}(q)\ , \tag{B4}$$

which differs from the expression used in previous applications of the RIA model[16–19] by the extra $R(q)$ factor. Equation (B4) may be conveniently reexpressed as

$$\Upsilon_{\rm Breit}(q)=-\frac{2\pi(\hbar c)^2}{m}\frac{R(q)}{R(0)}\frac{P_{\rm lab}}{P_{\rm NN\,c.m.}}F_{\rm NN\,c.m.}(q)\ , \tag{B5}$$

where $P_{\rm lab}$ is the laboratory momentum of the incident proton and $R(q=0)=P_{\rm lab}/\bar{k}_0$.

The ratio $R(q)/R(0)$ increases monotonically with increasing q. Typical values of $R(q)/R(0)$ are 1.02, 1.08, 1.17, and 1.30 at $q=1$, 2, 3, and 4 fm^{-1} for p + ^{40}Ca at

500 MeV. This enhancement of the large Fourier components of the NN effective interaction increases the large angle pA differential cross sections somewhat, resulting in improved descriptions of the data for most cases. The most significant effect of these kinematics occurs for light targets such as ^{12}C and ^{16}O for which $R(0)$ is typically 1.1. The magnitudes of the predicted RIA differential cross sections are increased resulting in better agreement with the data when the $R(q)$ factor is included.

The nonrelativistic t matrix appropriate for the NRIA model can similarly be obtained if the difference between the normalizations of the relativistic and nonrelativistic plane waves is recognized.[50] With

$$T(\text{nonrelativistic}) = m_1 m_2/(E_1 E_2 E_1' E_2')^{1/2} T(\text{relativistic}) ,$$

the relationship between the scattering amplitude and t matrix in the NRIA model is given by

$$t_{\text{NRIA}}(q) = -\frac{2\pi(\hbar c)^2}{E_p E_{\text{SN}}/m} \frac{R(q)}{R(0)} \frac{P_{\text{lab}}}{P_{\text{NN c.m.}}} f_{\text{NN c.m.}}(q) , \quad \text{(B6)}$$

which, for the cases considered here, is numerically equivalent to the kinematic part of Eq. (35), traditionally used in NRIA-Breit kinematic frame calculations.

[1]K. M. Watson, Phys. Rev. **89**, 575 (1953).

[2]A. K. Kerman, H. McManus, and R. M. Thaler, Ann. Phys. (N.Y.) **8**, 551 (1959).

[3]R. J. Glauber, in *Lectures in Theoretical Physics,* edited by W. E. Brittin and L. G. Dunham (Interscience, New York, 1959), p. 315.

[4]J. P. Jeukenne, A. Lejeune, and C. Mahaux, Phys. Rev. C **10**, 1391 (1974).

[5]H. V. von Geramb, in *The Interaction Between Medium Energy Nucleons in Nuclei—1982,* Proceedings of the Workshop on the Interaction Between Medium Energy Nucleons in Nuclei, (Indiana University Cyclotron Facility), AIP Conf. Proc. No. 97, edited by H. O. Meyer (AIP, New York, 1983), p. 44; L. Rikus and H. V. von Geramb, Nucl. Phys. **A426**, 496 (1984).

[6]L. Ray, in *The Interaction Between Medium Energy Nucleons in Nuclei—1982,* Proceedings of the Workshop on the Interaction Between Medium Energy Nucleons in Nuclei (Indiana University Cyclotron Facility), AIP Conf. Proc. No. 97, edited by H. O. Meyer (AIP, New York, 1983), p. 121.

[7]L. Ray, Phys. Rev. C **19**, 1855 (1979); L. Ray, W. R. Coker, and G. W. Hoffmann, *ibid.* C **18**, 2641 (1978).

[8]G. W. Hoffmann *et al.*, Phys. Rev. Lett. **47**, 1436 (1981).

[9]D. A. Hutcheon *et al.*, Phys. Rev. Lett. **47**, 315 (1981).

[10]A. Rahbar *et al.*, Phys. Rev. Lett. **47**, 1811 (1981).

[11]J. A. McNeil, L. Ray, and S. J. Wallace, Phys. Rev. C **27**, 2123 (1983).

[12]G. W. Hoffmann *et al.*, Phys. Rev. C **24**, 541 (1981).

[13]M. L. Barlett, W. R. Coker, G. W. Hoffmann, and L. Ray, Phys. Rev. C **29**, 1407 (1984).

[14]L. Ray (unpublished).

[15]B. C. Clark, S. Hama, and R. L. Mercer, in *The Interaction Between Medium Energy Nucleons in Nuclei—1982,* Proceedings of the Workshop on the Interaction Between Medium Energy Nucleons in Nuclei (Indiana University Cyclotron Facility), AIP Conf. Proc. No. 97, edited by H. O. Meyer (AIP, New York, 1983), p. 260. Elimination of the lower components of the wave function in the Dirac equation yields, after a transformation, a second-order Schrödinger equation in which the effective central and spin-orbit potentials are identifiable. The nonlinear density contributions to this effective NR optical potential include the virtual pair effects discussed in Appendix A.

[16]J. A. McNeil, J. Shepard, and S. J. Wallace, Phys. Rev. Lett. **50**, 1439 (1983).

[17]J. Shepard, J. A. McNeil, and S. J. Wallace, Phys. Rev. Lett. **50**, 1443 (1983).

[18]B. C. Clark, S. Hama, R. L. Mercer, L. Ray, and B. D. Serot, Phys. Rev. Lett. **50**, 1644 (1983).

[19]B. C. Clark, S. Hama, R. L. Mercer, L. Ray, G. W. Hoffmann, and B. D. Serot, Phys. Rev. C **28**, 1421 (1983); and (unpublished).

[20]J. D. Walecka, Ann. Phys. (N.Y.) **83**, 491 (1974).

[21]R. A. Arndt *et al.*, Phys. Rev. D **28**, 97 (1983); R. A. Arndt, private communication.

[22]W. G. Love and M. A. Franey, Phys. Rev. C **24**, 1073 (1981).

[23]E. E. van Faassen and J. A. Tjon, Phys. Rev. C **30**, 285 (1984).

[24]S. J. Wallace and J. A. Tjon, private communication.

[25]C. J. Horowitz, private communication.

[26]C. J. Horowitz, in *The Interaction Between Medium Energy Nucleons in Nuclei—1982,* Proceedings of the Workshop on the Interaction Between Medium Energy Nucleons in Nuclei (Indiana University Cyclotron Facility), AIP Conf. Proc. No. 97, edited by H. O. Meyer (AIP, New York, 1983), p. 329.

[27]R. M. Thaler, in Proceedings of the Third LAMPF II Workshop, edited by J. C. Allred, T. S. Bhatia, K. Ruminer, and B. Talley, Los Alamos National Laboratory Conference Report LA-9933-C, Vol. 1, p. 200; M. V. Hynes, A. Picklesimer, P. C. Tandy, and R. M. Thaler, Phys. Rev. C (to be published); see also Ref. 33.

[28]J. D. Bjorken and S. D. Drell, *Relativistic Quantum Mechanics* (McGraw-Hill, New York, 1964).

[29]C. J. Horowitz and B. D. Serot, Nucl. Phys. **A368**, 503 (1981).

[30]M. J. Moravcsik, *The Two-Nucleon Interaction* (Clarendon, Oxford, 1963), pp. 11–18.

[31]M. Morita, *Beta Decay and Muon Capture* (Benjamin, London, 1973), pp. 15–17.

[32]M. L. Goldberger, Y. Nambu, and R. Oehme, Ann. Phys. (N.Y.) **2**, 226 (1957).

[33]M. V. Hynes, A. Picklesimer, P. C. Tandy, and R. M. Thaler, Phys. Rev. Lett. **52**, 978 (1984).

[34]A. Picklesimer, P. C. Tandy, R. M. Thaler, and D. H. Wolfe, Phys. Rev. C **29**, 1582 (1984); **30**, 1861 (1984).

[35]E. D. Cooper, Ph.D. thesis, University of Alberta, 1981 (unpublished).

[36]I. Sick *et al.*, Phys. Lett. **88B**, 245 (1979); H. J. Emrich *et al.*, Nucl. Phys. (to be published).

[37]B. Frois *et al.*, Phys. Rev. Lett. **38**, 152 (1977).

[38]W. Bertozzi, J. Friar, J. Heisenberg, and J. W. Negele, Phys.

Lett. **41B**, 408 (1972).

[39]J. Dechargé and D. Gogny, Phys. Rev. C **21**, 1568 (1980); J. Dechargé, M. Girod, D. Gogny, and B. Grammaticos, Nucl. Phys. **A358**, 203c (1981); J. Dechargé, private communication.

[40]B. C. Clark *et al.*, Phys. Rev. Lett. **51**, 1808 (1983).

[41]L. Ray, G. W. Hoffmann, and R. M. Thaler, Phys. Rev. C **22**, 1454 (1980).

[42]The 300 MeV ^{40}Ca and ^{208}Pb data and the 400 MeV ^{40}Ca TRIUMF data are from D. A. Hutcheon *et al.*, private communication. The 400 MeV ^{208}Pb TRIUMF data are published in Ref. 9. The 500 MeV Los Alamos Meson Physics Facility—high resolution spectrometer (LAMPF-HRS) data are published in Ref. 8. The 613 MeV Saclay cross section data are from the tabulation of G. Bruge, Saclay Report DPh-N/ME/78-1, 1978 (unpublished). The 800 MeV ^{40}Ca HRS cross section data are published in Ref. 44 and the analyzing power data are presented in G. Igo *et al.*, Phys. Lett. **81B**, 151 (1979). The 800 MeV ^{208}Pb HRS cross section data appear in G. W. Hoffmann *et al.*, Phys. Rev. C **21**, 1488 (1980) and the analyzing power data are given in Ref. 12. The 1 GeV ^{40}Ca cross section data from Saclay are in G. D. Alkhazov *et al.*, Nucl. Phys. **A274**, 443 (1976). The 1 GeV ^{208}Pb cross section data from Gatchina are presented in G. D. Alkhazov *et al.*, Izv. Akad. Nauk. SSSR Ser. Fiz. **244**, 3 (1976). The 1 GeV polarization data of Gatchina are published in G. D. Alkhazov *et al.*, Phys. Lett. **90B**, 364 (1980). The 500 MeV p + ^{40}Ca HRS spin rotation data are from Ref. 10, while the ^{208}Pb Q data are from B. Aas *et al.*, Bull. Am. Phys. Soc. **26**, 1125 (1981); and B. Aas, private communication. The HRS ^{48}Ca cross section data at 500 and 800 MeV are from Refs. 8 and 44, respectively.

[43]G. W. Hoffmann *et al.* (unpublished).

[44]L. Ray *et al.*, Phys. Rev. C **23**, 828 (1981).

[45]L. Ray and G. W. Hoffmann, Phys. Rev. C **27**, 2143 (1983).

[46]We have also applied the RIA model to preliminary 800 MeV spin rotation data for ^{16}O and ^{40}Ca targets (R. W. Fergerson *et al.*, private communication) with successful descriptions resulting.

[47]R. J. Glauber and P. Osland, Phys. Lett. **80B**, 401 (1979).

[48]A. Bernstein and R. A. Miskimen, private communication.

[49]S. J. Wallace, in *Advances in Nuclear Physics,* edited by J. W. Negele and E. Vogt (Plenum, New York, 1981), Vol. 12, p. 135.

[50]J. J. Sakurai, *Advanced Quantum Mechanics,* (Addison-Wesley, London, 1967), p. 312.